ON FLEXIBLE TUBES CONVEYING A MOVING FLUID: VARIATIONAL DYNAMICS AND SPECTRAL ANALYSIS

by

Mitchell Harrison Canham

A thesis submitted in partial fulfillment of the requirements for the degree of

Master of Science

in

Applied Mathematics

Department of Mathematical and Statistical Sciences

University of Alberta

Abstract

This study focuses on the motion of a hollow flexible tube conveying a flowing fluid, also known as the garden-hose instability. This system becomes unstable when the fluid moving through the pipe exceeds a critical flow rate. This non-linear dynamical system involves complex fluid-structure interactions. As the fluid travels down the pipe it can cause deformations to the pipe structure, which consequently changes the flow dynamics. Research into this system began with the work of Ashley and Haviland (1950), who were attempting to explain vibrations which show up in pipelines. It has since garnered considerable interest in scientific literature as it has numerous practical applications. It can be used to model biomechanical systems such as blood flow through arteries or airflow through alveoli in the lungs. It also has applications to aerospace designs as early stage rocket engines require rapid transfer of enormous quantities of fuel through relatively thin and lightweight pipes.

My research involves creating a simple model of a hollow tube conveying a fluid and investigating the ordinary differential equations that get produced. This model uses a geometrically exact theory that takes into consideration a tube that has a variable cross section in space and time. This theory is derived in a Lagrangian variational framework.

I will also present a physical experiment I created of a flexible tube conveying water. Data is collected from the experiment using a stereoscopic camera set up and a centerline detection algorithm. I suggest a means to analyze this type of data using a Koopman operator, which has never been previously used to investigate the dynamics of the garden hose instability.

Preface

This thesis is an original work by Mitchell Canham. An image used in this thesis was presented at the Gallery of Fluid Motion during the 67th Annual Meeting of the APS Division of Fluid Dynamics in San Francisco, California.

Acknowledgements

I would first like to thank my graduate supervisor, Dr. Vakhtang Putkaradze of the Department of Mathematical and Statistical Sciences at the University of Alberta. Prof. Putkaradze was always there to answer my questions and review my work. He provided me with the motivation and means to achieve what I never thought was possible.

I would also like to express my gratitude to Dr. David Nobes of the Department of Mechanical Engineering at the University of Alberta. Prof. Nobes was extremely generous letting me use his lab to run my very wet and messy experiments in the midst of expensive equipment. He supplied me with all the materials and expertise needed to get the experiment running successfully.

Last but not least, I would like to thank Mandi Paton for relentless encouragement, my family for unwavering support, Nathan Croswell for thought-provoking discussions, and Yoshi for waking me up every morning.

Thank You.

Mitchell Canham

Table of Contents

List of Figures

1 Introduction

When a fluid passes through a tube or pipe at a high enough flux it causes instability. This instability can be directly observed. If the tube is flexible enough, one can observe an erratic, almost chaotic looking motion of the tube, or if the tube is more stiff like a steel pipe, small vibrations can be observed. This instability is commonly referred to as the *Garden Hose Instability*. This system involves complex fluid-structure interactions. When the fluid flows through the tube, the walls of the tube get deformed, which consequently affects how the fluid is flowing through pipe, which in turn deforms the wall again in a different manner. Work in this field began when vibration problems arose in the transportation of oil through pipelines. This has obvious environmental considerations as vibrations can cause the pipeline to burst or leak. Ashley and Haviland [1] first investigated this system in 1950 using a simple supported horizontal beam to look at the vibrations. This system has many other real world extensions. Models of blood flowing through arteries could rely on this theory, or air flowing through the structures of the lungs. It also has important applications to rocket engine design, as launch vehicles for space ships require huge quantities of fuel passing at high speed through thin walled pipes to get to the rocket engines. Vibrations in these pipes could lead to catastrophic failure of the rocket so these applications provided some motivation for developing the theory.

There has been extensive research done in this field. In 1961 Benjamin [2, 3] utilized a variational method to describe the dynamics of a chain of articulated pipes in what was one of the most important contributions to the study of this system. Paidoussis [13–16] has also done extensive work into this system of axial flow through slender structures.

This thesis is broken down into 2 main parts. The first part of this thesis lies in Section 3 and is an original contribution. It consists of the derivation and analysis of a simple discrete model of a stretching tube using a variational framework. In this part, we utilize the continuous variational theory developed in [5, 6]. These articles lay out the Lagrangian structure and utilize a geometrically exact approach that can deal with a dynamically changing cross-sectional area which changes in both space and time. One of the main issues with previous approaches was how to describe the change in cross-sectional area of a collapsable tube.

Previous works have considered a quasi-static approximation of the change in cross-sectional area by $uA = constant$, where u is the flow rate of the fluid and A is the cross-sectional area of the tube [8, 12, 15, 18]. In general, this approximation does not correctly describe the dynamics.

Gay-Balmaz and Putkaradze [7] derive the discrete conservation laws from the geometrically exact theory using variational integration. The discrete conservation laws form a closed system and are discrete analogs of the continuous conservation laws. This discretization allows for consistent approximations of numerical solutions. It is with these discrete conservation laws that we base the model. After obtaining the equations of motion from the model, we linearize the system and study the linear stability.

The second part of this thesis is in Section 5 with the experiment I created and analysed using a novel method that has never before been used to investigate tube dynamics. This section is also an original contribution. The experiment consists of a vertically suspended flexible tube connected to a water source where the flow rate of water can be controlled and measured. The collection of data involves using stereoscopic imaging and a simple object recognition algorithm to obtain the 3D shape of the tube. After that, I will explain the Koopman operator, an infinite dimensional linear operator which allows one to perform spectral analysis on a non-linear dynamical system without linearization. Although the operator is linear it still captures the full non-linear dynamics of the system. A thorough review of the Koopman operator is available in [4]. This framework allows one to analyse dynamical systems that are otherwise poorly described using observable data. Previous work [9–11, 17] has been done utilizing the Koopman operator to analyse flow dynamics by breaking down the flow structures into modes. These modes automatically identify coherent structures in flows. This method requires no knowledge of the Koopman operator, as the modes of decomposition can be calculated using snapshots in time of empirical data from observable quantities in the system. In some of the previous works, the observable quantity has been flow fields obtained through particle image velocimetry (PIV). I present a method that instead uses the position vectors of the tube, obtained via a stereoscopic camera, as the empirical snapshots. This has never been done before to analyse the dynamics of a fluid-conveying flexible tube.

1.1 Variational Integrators

Variational integration is a numerical method that can be used to approximate the solutions to ordinary differential equations (ODE). Variational integrators are geometric integrators of a discretized Lagrangian. Numerical integration refers to using numerical methods to find approximations to the solutions of differential equations. Mathematical models that model how physical systems change in time are called dynamical systems and they are typically a system of differential equations. Variational integrators are useful in that they conserve momentum and are symplectic. Symplectic integrators preserve energy in the system as they conserve a Hamiltonian. This is useful for long term behaviour as one does not want large changes in energy which can cause the approximation to diverge from the actual solution. Geometric integrators use the geometric structure of the dynamical system to find a numerical solution. If we look at the dynamics of the system in a variational way using a Lagrangian or Hamiltonian, then we can use a variatonal integrator which discretizes the variational representation of the system. This can provide a solution for many mechanical systems. This information is best described using examples. However, we will first look at variational Lagrangian dynamics in the continuous case before we consider examples of the discrete case for variational integration.

To create a simple variational integrator, we first construct the Lagrangian to describe the mechanical system, typically the kinetic energy subtracted by the potential energy. Take for example this simple mechanical system:

$$L\left(q,\dot{q}\right)=K\left(\dot{q}\right)-U\left(q\right)=\frac{1}{2}m\dot{q}^{2}-U\left(q\right) \tag{1.1}$$

Where K and U are functions for the kinetic and potential energy resepectively, m is the mass and q is a coordinate of the system, for example the spatial position. Next we must consider the action of the system. In mechanics the action of a physical system is a functional from which the equations of motion can be derived. In this case the action takes the form of a time integral of the Lagrangian over the path $q\left(t\right)$:

$$S\left(q\right)=\int_{0}^{T}L(q\left(t\right),\dot{q}\left(t\right),t)\ \mathrm{d}t \tag{1.2}$$

Hamilton's principle states that the true path of the system is a stationary point of the action functional. In other words, the action integral of the true evolution of the system

remains unchanged to first order perturbations of the coordinates.

$$\delta S = 0 \tag{1.3}$$

Using this principle we can create the famous Euler-Lagrange equations which can be used to find the equations of motion of a dynamical system. We first must calculate the variations of the action functional δS for variations δq of $q(t)$. Let $q(t)$ be the true evolution of the system, we define a function $p(t, \epsilon)$ that parameterizes variations from the true path. If we say $\delta q(t)$ is defined for all t and $\delta q(0) = \delta q(T) = 0$ then:

$$p(t, \epsilon) = q(t) + \epsilon \cdot \delta q(t) \tag{1.4}$$

$$S[\epsilon] = \int_0^T L(p(t, \epsilon), \dot{p}(t, \epsilon), t)\, \mathrm{d}t \tag{1.5}$$

When $\epsilon = 0$ we get a stationary point of the action $S[\epsilon]$ by Hamilton's principle and construction of p, therefore we know that:

$$\delta S[\epsilon]\Big|_{\epsilon=0} = 0 \tag{1.6}$$

Computing $\delta S[\epsilon]$:

$$\delta S[\epsilon]\Big|_{\epsilon=0} = \frac{\partial S}{\partial \epsilon}\Big|_{\epsilon=0} = \int_0^T \left[\frac{\partial L}{\partial p}\frac{\partial p}{\partial \epsilon} + \frac{\partial L}{\partial \dot{p}}\frac{\partial \dot{p}}{\partial \epsilon}\right] \mathrm{d}t\Big|_{\epsilon=0} \tag{1.7}$$

$$\frac{\partial p}{\partial \epsilon} = \delta q(t), \quad \frac{\partial \dot{p}}{\partial \epsilon} = \delta \dot{q}(t) \tag{1.8}$$

Since $\frac{\partial L}{\partial p}\Big|_{\epsilon=0} = \frac{\partial L}{\partial q}$ we get:

$$\delta S[\epsilon] = \int_0^T \left[\delta q \frac{\partial L}{\partial q} + \delta \dot{q}\frac{\partial L}{\partial \dot{q}}\right] \mathrm{d}t \tag{1.9}$$

Now we perform integration by parts on the term $\delta \dot{q}\frac{\partial L}{\partial \dot{q}}$ to arrive at:

$$\delta S[\epsilon] = \int_0^T \delta q \frac{\partial L}{\partial q}\mathrm{d}t + \delta q \frac{\partial L}{\partial \dot{q}}\Big|_0^T - \int_0^T \delta q \frac{d}{dt}\left(\frac{\partial L}{\partial \dot{q}}\right) \tag{1.10}$$

Since $\delta q(0) = \delta q(T) = 0$, the middle term vanishes and we are left with:

$$\delta S[\epsilon] = \int_0^T \delta q \cdot \left(\frac{\partial L}{\partial q} - \frac{d}{dt}\frac{\partial L}{\partial \dot{q}}\right) \mathrm{d}t \tag{1.11}$$

$\delta S\left[\epsilon\right]\Big|_{\epsilon=0} = 0$ must hold true for any choice of the arbitrary δq. This is the case if and only if:

$$\frac{\partial L}{\partial q} - \frac{d}{dt}\frac{\partial L}{\partial \dot{q}} = 0 \tag{1.12}$$

The above equation is known as the Euler-Lagrange equation and it provides the continuous equations of motion for the variable q.

We now turn our attention away from continuous variational dynamics to discrete variational integration. We first must form the discrete Lagrangian. The discrete Lagrangian is a simple numerical approximation of the action of the system over a short time step. Since the action in the continuous case is a definite integral, it is typical to use quadrature to get a discrete Lagrangian. Different numerical methods can be used to discretize certain parts of the Lagrangian, such as the trapezoid method or the Euler method with finite difference approximations. Here we use the trapezoidal method to approximate the action integral:

$$\int_{t_i}^{t_{i+1}} L(q\left(t\right), \dot{q}\left(t\right), t)\ \mathrm{d}t \approx \frac{h_i}{2}\left(L\left[t_i, q_i, \dot{q_i}\right] + L\left[t_{i+1}, q_{i+1}, \dot{q_{i+1}}\right]\right) \tag{1.13}$$

Where h_i is the time-step between t_i and t_{i+1}. We can then use the finite difference approximation:

$$\dot{q_i} \approx \frac{q_{i+1} - q_i}{h_i} \tag{1.14}$$

Assuming that (1.14) is the constant velocity between t_i and t_{i+1} we arrive at our discrete Lagrangian:

$$\hat{L} = \frac{h_i}{2}\left(L\left[t_i, q_i, \frac{q_{i+1} - q_i}{h_i}\right] + L\left[t_{i+1}, q_{i+1}, \frac{q_{i+2} - q_{i+1}}{h_{i+1}}\right]\right) \tag{1.15}$$

The choice of numerical method used for discretization will result in a different variational integrator. The accuracy of the variational integrator will depend on the accuracy of the numerical scheme used to approximate the action. To find the equations of motion over a long time interval, the discrete Langrangians are summed over many short time steps. This is called the discrete action. We will now see how a variational integrator preserves the energy of a system compared to an implicit Euler method. We will look a the simple system of a particle in a potential with the Lagrangian:

$$L\left(x\right) = \frac{1}{2}m\dot{x}^2 - \frac{1}{2}kx^2 \tag{1.16}$$

This is the well known mass-spring model or harmonic oscillator with linear restoring force and no damping force. Applying the Euler-Lagrange equation we get:

$$m\ddot{x} = -kx \tag{1.17}$$

Converting the second-order ordinary differential equation (ODE) into a system of first-order ODEs:

$$\dot{x} = v \tag{1.18}$$

$$\dot{v} = -\frac{kx}{m} \tag{1.19}$$

Using a forward Euler method we get:

$$\begin{aligned} x_{i+1} &= x_i + hv_i \\ v_{i+1} &= v_i - \frac{hkx_i}{m} \end{aligned} \tag{1.20}$$

Hamilton's principle states that the correct path of a dynamical system is one where the path is a stationary point. In other words small first-order variations to the coordinates leave the action unchanged, where the variation is 0 at the endpoints. This holds true in the discrete case as well.

Now, let us construct a variational integrator and compare it to (1.20). The first step to create the variational integrator is to construct the discrete Lagrangian.

$$L_d\left(x_i\right) = \frac{m}{2}\left(\frac{x_{i+1} - x_i}{h}\right)^2 - \frac{k}{2}x_i^2 \tag{1.21}$$

Next, we use the discrete Euler Lagrange equations to get the equation of motion:

$$\frac{m}{h^2}\left(x_{i+1} - 2x_i + x_{i-1}\right) + kx_i = 0 \tag{1.22}$$

$$x_{i+1} = \left(2 - \frac{kh^2}{m}\right)x_i - x_{i-1} \tag{1.23}$$

Now we will compare the trajectories of these two systems in Figure 1.1. For these simulations, $m = 1$, $k = 1$, and $h = 0.5$. They were run over 1000 timesteps with initial conditions $(x_0, v_0) = (0, 1)$. One can see how the variational integrator oscillates as expected with constant amplitude, while the Euler method begins to explode as it oscillates with increasing

Figure 1.1 Numerically computed trajectory of a harmonic oscillator with linear restoring force and no damping force, comparing a variational integrator to an Euler method.

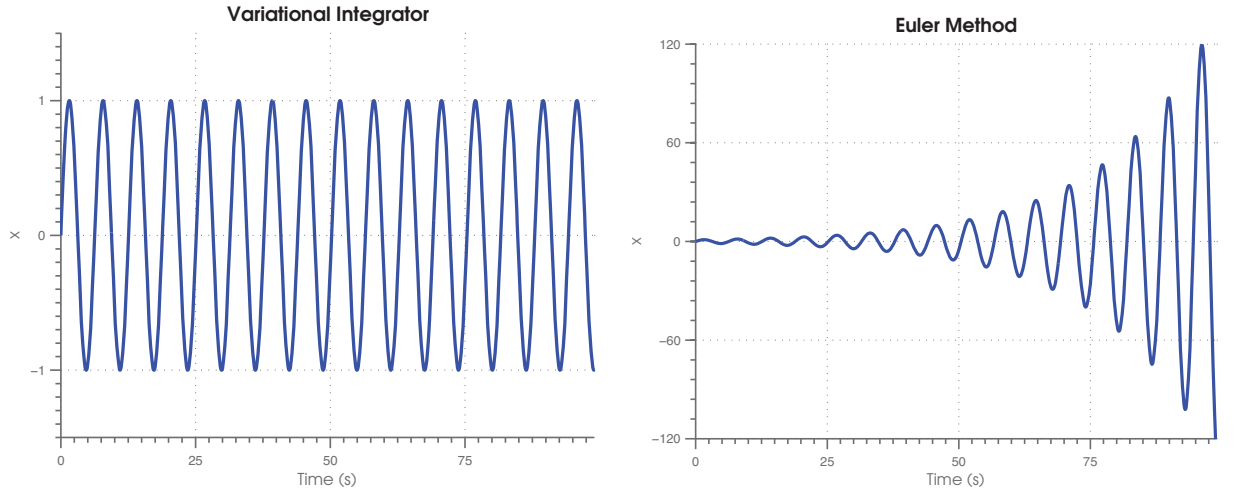

(a) Trajectory of a variational integrator.

(b) Trajectory of an Euler method.

amplitude over a relatively short time interval. This is further illustrated in Figure 1.2. The total energy of this system should be conserved. Although the energy is not conserved for the variational integrator, it oscillates with small unchanging amplitude. Over long enough time intervals the average energy of the system is constant. The Euler method on the other hand quickly gains energy and explodes, which is not a desirable result.

1.1.1 Variational integration with holonomic constraints

Holonomic constraints provide a relation between the coordinates of a mechanical system and take the form: $F(\mathbf{q}) = 0$. Let's consider the 2-dimensional case of a particle in a potential $U(x, y)$ where $\mathbf{q} = \{x, y\}$. If we let $F(\mathbf{q}) = x^2 + y^2 - 1$, then the system is constrained to a circle like a pendulum. The continuous Lagrangian of this system becomes:

$$L = \frac{m}{2}\left(\dot{x}^2 + \dot{y}^2\right) - U(x, y) - \lambda\left(x^2 + y^2 - 1\right) \tag{1.24}$$

where λ is a Lagrange multiplier. Applying the Euler-Lagrange equations to this Lagrangian we get:

$$m\ddot{x} + \frac{\partial U}{\partial x} = -2\lambda x$$
$$m\ddot{y} + \frac{\partial U}{\partial y} = -2\lambda y$$

Figure 1.2 Total energy of a numerically computed harmonic oscillator with linear restoring force and no damping, comparing a variational integrator to an Euler method.

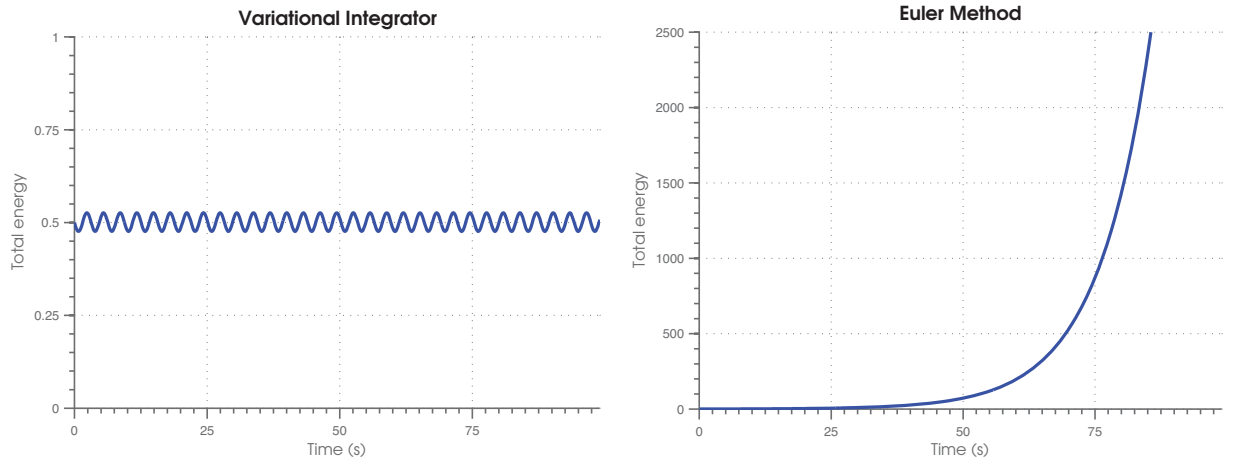

(a) Total energy of a variational integrator. **(b)** Total energy of an Euler method.

If we let $U = \frac{k}{2}\left(x^2 + y^2\right)$ then the equations of motion become:

$$m\ddot{x} + kx = -2\lambda x \tag{1.25}$$

$$m\ddot{y} + ky = -2\lambda y \tag{1.26}$$

If we multiply (1.25) by x and (1.26) by y we get:

$$mx\ddot{x} + kx^2 = -2\lambda x^2 \tag{1.27}$$

$$my\ddot{y} + ky^2 = -2\lambda y^2 \tag{1.28}$$

Combining these equations and the fact that $x^2 + y^2 = 1$ from the constraint:

$$m\left(x\ddot{x} + y\ddot{y}\right) + k = -2\lambda \tag{1.29}$$

We want to try to remove second derivatives, so we take the 2nd time derivative of the constraint $x^2 + y^2 = 1$:

$$2x\dot{x} + 2y\dot{y} = 0 \tag{1.30}$$

$$2\dot{x}^2 + 2x\ddot{x} + 2\dot{y}^2 + 2y\ddot{y} = 0 \tag{1.31}$$

$$x\ddot{x} + y\ddot{y} = -\left(\dot{x}^2 + \dot{y}^2\right) \tag{1.32}$$

If we take (1.32) into (1.29) and solve for λ we get:

$$\lambda = \frac{1}{2}\left(m\left(\dot{x}^2 + \dot{y}^2\right) - k\right) \tag{1.33}$$

We also get a conservation law if we instead multiply (1.25) by $\dot{x}$, (1.26) by $\dot{y}$ and combine the equations:

$$m\left(\dot{x}\ddot{x} + \dot{y}\ddot{y}\right) = -\left(x\dot{x} + y\dot{y}\right)\left(k + 2\lambda\right) \tag{1.34}$$

The left-hand side of this equation is the time derivative of the kinetic energy T, and the right hand side of this equation becomes 0 using (1.30), therefore:

$$\frac{dT}{dt} = m\left(\dot{x}\ddot{x} + \dot{y}\ddot{y}\right) = 0 \tag{1.35}$$

Therefore kinetic energy is conserved in this system.

Next we will compare different numerical schemes to variational integration. First we convert (1.27) and (1.28) to a first order system of differential equations by letting:

$$Y = \begin{pmatrix} x \\ y \\ \dot{x} \\ \dot{y} \end{pmatrix} = \begin{pmatrix} Y_1 \\ Y_2 \\ Y_3 \\ Y_4 \end{pmatrix} \tag{1.36}$$

Differentiating and using (1.27) and (1.28):

$$\frac{dY}{dt} = \begin{pmatrix} Y_3 \\ Y_4 \\ -\frac{1}{m}\left(2\lambda + k\right)Y_1 \\ -\frac{1}{m}\left(2\lambda + k\right)Y_2 \end{pmatrix} = F\left(Y\right) \tag{1.37}$$

Where:

$$\lambda = \frac{1}{2}\left(m\left(Y_3^2 + Y_4^2\right) - k\right) \tag{1.38}$$

Simplification of (1.37) leads to:

$$F\left(Y\right) = \begin{pmatrix} Y_3 \\ Y_4 \\ -Y_1\left(Y_3^2 + Y_4^2\right) \\ -Y_2\left(Y_3^2 + Y_4^2\right) \end{pmatrix} \tag{1.39}$$

An explicit Euler method to solve this system numerically is as follows:

$$Y^{n+1} = Y^n + h \cdot F\left(Y^n\right) \tag{1.40}$$

We will also look at a 4th-order Runge-Kutta method:

$$Y^{n+1} = Y^n + \frac{h}{6}\left(k_1 + 2k_2 + 2k_3 + k_4\right) \tag{1.41}$$

Where:

$$k_1 = F\left(Y^n\right) \tag{1.42}$$

$$k_2 = F\left(Y^n + \frac{h}{2}k_1\right) \tag{1.43}$$

$$k_3 = F\left(Y^n + \frac{h}{2}k_2\right) \tag{1.44}$$

$$k_4 = F\left(Y^n + hk_3\right) \tag{1.45}$$

We will compare these 2 well known numerical schemes to a variational integrator. The first step is to set up the discrete Lagrangian from the continuous one in (1.24), letting $\mathbf{q}_i = (x_i, y_i)$ and using a general potential energy $U(x_i, y_i)$:

$$\begin{aligned} &L_d\left(\mathbf{q}_i, \frac{\mathbf{q}_{i+1} - \mathbf{q}_i}{h}\right) \\ &\quad = \frac{m}{2}\left[\left(\frac{x_{i+1} - x_i}{h}\right)^2 + \left(\frac{y_{i+1} - y_i}{h}\right)^2\right] - U\left(x_i, y_i\right) - \lambda_i\left(x_i^2 + y_i^2 - 1\right) \end{aligned} \tag{1.46}$$

with holonomic constraint:

$$F\left(\mathbf{q}_i\right) = x_i^2 + y_i^2 - 1 = 0 \tag{1.47}$$

A forward difference method was used to approximate the time derivative. Next we use the discrete Euler-Lagrange equations and a central difference approximation for the 2nd-order time derivative to get the equations of motion:

$$\frac{m}{h^2}\left(x_{i+1} - 2x_i + x_{i-1}\right) + \frac{\partial U}{\partial x_i} + 2\lambda_i x_i = 0 \tag{1.48}$$

$$\frac{m}{h^2}\left(y_{i+1} - 2y_i + y_{i-1}\right) + \frac{\partial U}{\partial y_i} + 2\lambda_i y_i = 0 \tag{1.49}$$

Multiplying (1.48) by x_i, (1.49) by y_i, and adding together we get:

$$\frac{m}{h^2}\left[\left(x_{i+1} - 2x_i + x_{i-1}\right)x_i + \left(y_{i+1} - 2y_i + y_{i-1}\right)y_i\right] = -\frac{\partial U}{\partial x_i}x_i - \frac{\partial U}{\partial y_i}y_i - 2\lambda_i\left(x_i^2 + y_i^2\right) \tag{1.50}$$

Simplifying using (1.47):

$$2\lambda = -\frac{m}{h^2}\left(x_{i+1}x_i + x_{i-1}x_i + y_{i+1}y_i + y_{i-1}y_i - 2\right) - \frac{\partial U}{\partial x_i}x_i - \frac{\partial U}{\partial y_i}y_i \tag{1.51}$$

Substituting (1.51) into (1.48) and (1.49) we get:

$$\begin{aligned}\frac{m}{h^2}\left(x_{i+1} - 2x_i + x_{i-1}\right) + \frac{\partial U}{\partial x_i} - \frac{m}{h^2}x_i\left(x_{i+1}x_i + x_{i-1}x_i + y_{i+1}y_i + y_{i-1}y_i - 2\right)\\ - \frac{\partial U}{\partial x_i}x_i^2 - \frac{\partial U}{\partial y_i}x_iy_i = 0\end{aligned} \tag{1.52}$$

$$\begin{aligned}\frac{m}{h^2}\left(y_{i+1} - 2y_i + y_{i-1}\right) + \frac{\partial U}{\partial y_i} - \frac{m}{h^2}y_i\left(x_{i+1}x_i + x_{i-1}x_i + y_{i+1}y_i + y_{i-1}y_i - 2\right)\\ - \frac{\partial U}{\partial y_i}y_i^2 - \frac{\partial U}{\partial x_i}x_iy_i = 0\end{aligned} \tag{1.53}$$

Simplifying:

$$\frac{m}{h^2}\left(x_{i+1}\left(1 - x_i^2\right) - y_{i+1}\left(x_iy_i\right) + x_{i-1}\left(1 - x_i^2\right) - y_{i-1}x_iy_i\right) + \frac{\partial U}{\partial x_i}\left(1 - x_i^2\right) - \frac{\partial U}{\partial y_i}x_iy_i = 0 \tag{1.54}$$

$$\frac{m}{h^2}\left(y_{i+1}\left(1 - y_i^2\right) - x_{i+1}\left(x_iy_i\right) + y_{i-1}\left(1 - y_i^2\right) - x_{i-1}x_iy_i\right) + \frac{\partial U}{\partial y_i}\left(1 - y_i^2\right) - \frac{\partial U}{\partial x_i}x_iy_i = 0 \tag{1.55}$$

Using the constraint, $y_i^2 = 1 - x_i^2$ and $x_i^2 = 1 - y_i^2$:

$$\frac{m}{h^2}\left(x_{i+1}y_i^2 - y_{i+1}\left(x_iy_i\right) + x_{i-1}y_i^2 - y_{i-1}x_iy_i\right) + \frac{\partial U}{\partial x_i}y_i^2 - \frac{\partial U}{\partial y_i}x_iy_i = 0 \tag{1.56}$$

$$\frac{m}{h^2}\left(y_{i+1}x_i^2 - x_{i+1}\left(x_iy_i\right) + y_{i-1}x_i^2 - x_{i-1}x_iy_i\right) + \frac{\partial U}{\partial y_i}x_i^2 - \frac{\partial U}{\partial x_i}x_iy_i = 0 \tag{1.57}$$

Solving for x_{i+1} and y_{i+1}:

$$x_{i+1} = \frac{y_{i+1}x_i}{y_i} - x_{i-1} + \frac{y_{i-1}x_i}{y_i} + \frac{h^2}{m}\left(\frac{\partial U}{\partial y_i}\frac{x_i}{y_i} - \frac{\partial U}{\partial x_i}\right) \tag{1.58}$$

$$y_{i+1} = \frac{x_{i+1}y_i}{x_i} - y_{i-1} + \frac{x_{i-1}y_i}{x_i} + \frac{h^2}{m}\left(\frac{\partial U}{\partial x_i}\frac{y_i}{x_i} - \frac{\partial U}{\partial y_i}\right) \tag{1.59}$$

Now, either (1.58) or (1.59) can be substituted into $x_{i+1}^2 + y_{i+1}^2 = 1$ to get a quadratic equation for y_{i+1} or x_{i+1} respectively:

$$x_{i+1}^2 + \left(\frac{x_{i+1}y_i}{x_i} - y_{i-1} + \frac{x_{i-1}y_i}{x_i} + \frac{h^2}{m}\left(\frac{\partial U}{\partial x_i}\frac{y_i}{x_i} - \frac{\partial U}{\partial y_i}\right)\right)^2 - 1 = 0 \tag{1.60}$$

$$y_{i+1}^2 + \left(\frac{y_{i+1}x_i}{y_i} - x_{i-1} + \frac{y_{i-1}x_i}{y_i} + \frac{h^2}{m}\left(\frac{\partial U}{\partial y_i}\frac{x_i}{y_i} - \frac{\partial U}{\partial x_i}\right)\right)^2 - 1 = 0 \tag{1.61}$$

An interesting characteristic of this scheme is that we get degeneracy, *i.e.* disappearance of the step-size h, when we have a central potential $U(r_i)$ at the origin, where $r_i = \sqrt{x_i^2 + y_i^2}$. For example, looking at the last term of (1.58) with a central potential $U(r_i)$ we get:

$$\begin{aligned}\frac{\partial U(r_i)}{\partial y_i}\frac{x_i}{y_i} - \frac{\partial U(r_i)}{\partial x_i} &= \frac{\partial U(r_i)}{\partial r_i}\frac{\partial r_i}{\partial y}\frac{x_i}{y_i} - \frac{\partial U(r_i)}{\partial r_i}\frac{\partial r_i}{\partial x_i} \\ &= \frac{\partial U}{\partial r_i}\frac{y_i}{\sqrt{x_i^2+y_i^2}}\frac{x_i}{y_i} - \frac{\partial U}{\partial r_i}\frac{x_i}{\sqrt{x_i^2+y_i^2}} \\ &= 0\end{aligned} \tag{1.62}$$

A similar argument follows for the last term in (1.59). To investigate this further, we can look at the exact solution for the central potential. If we write the Lagrangian in polar coordinates we get:

$$L = \frac{m}{2}\dot{\theta}^2 - \frac{kr^2}{2} - \lambda\left(r^2 - 1\right) \tag{1.63}$$

Applying the Euler-Lagrange equation in terms of θ:

$$m\ddot{\theta} = 0 \tag{1.64}$$

Solving this differential equation:

$$\theta(t) = c_1 t + c_2 \tag{1.65}$$

Since we know that $r = 1$, we can see that the particle will move with constant velocity in a circle, with the velocity depending on the initial conditions. This will be useful later.

A much simpler scheme involves converting this variational system to polar coordinates. First, rewriting (1.56):

$$x_{i+1}y_i^2 - y_{i+1}x_iy_i + x_{i-1}y_i^2 - y_{i-1}x_iy_i + \frac{h^2}{m}\left(\frac{\partial U}{\partial x_i}y_i^2 - \frac{\partial U}{\partial y_i}x_iy_i\right) = 0 \tag{1.66}$$

If we define $x_i = r_i\cos(\theta_i)$ and $y_i = r_i\sin(\theta_i)$ and substitute that into the constraint we get $r_i^2\cos^2(\theta_i) + r_i^2\sin^2(\theta_i) = 1$. Using the Pythagorean trigonometric identity we will define $r_i = 1$. Converting (1.66) into polar coordinates we get:

$$\begin{aligned}&\cos(\theta_{i+1})\sin^2(\theta_i) - \sin(\theta_{i+1})\cos(\theta_i)\sin(\theta_i) + \cos(\theta_{i-1})\sin^2(\theta_i) \\ &\quad - \sin(\theta_{i-1})\cos(\theta_i)\sin(\theta_i) + \frac{h^2}{m}\left(-\frac{\partial U}{\partial\theta_i}\sin^3(\theta_i) - \frac{\partial U}{\partial\theta_i}\cos^2(\theta_i)\sin(\theta_i)\right) = 0\end{aligned} \tag{1.67}$$

Where we used:

$$\frac{\partial U}{\partial x} = \cos(\theta)\frac{\partial U}{\partial r} - \frac{1}{r}\sin(\theta)\frac{\partial U}{\partial \theta}, \quad r = 1$$
$$\frac{\partial U}{\partial y} = \sin(\theta)\frac{\partial U}{\partial r} + \frac{1}{r}\cos(\theta)\frac{\partial U}{\partial \theta}, \quad r = 1$$

with r=1. We can see that $\sin(\theta_i)$ is common to all terms so we can pull it out of the equation and rearrange to get:

$$\begin{aligned}\cos(\theta_{i+1})\sin(\theta_i) - \cos(\theta_i)\sin(\theta_{i+1}) + \\ + \cos(\theta_{i-1})\sin(\theta_i) - \cos(\theta_i)\sin(\theta_{i-1}) - \frac{h^2}{m}\frac{\partial U}{\partial \theta_i} = 0\end{aligned} \tag{1.68}$$

Using the angle-difference trigonometric identity this simplifies to:

$$-\sin(\theta_{i+1} - \theta_i) + \sin(\theta_i - \theta_{i-1}) - \frac{h^2}{m}\frac{\partial U}{\partial \theta_i} = 0 \tag{1.69}$$

$$\sin(\theta_{i+1} - \theta_i) = \sin(\theta_i - \theta_{i-1}) - \frac{h^2}{m}\frac{\partial U}{\partial \theta_i} \tag{1.70}$$

$$\theta_{i+1} = \theta_i + \arcsin\left(\sin(\theta_i - \theta_{i-1}) - \frac{h^2}{m}\frac{\partial U}{\partial \theta_i}\right) \tag{1.71}$$

We now have an explicit solution for θ_{i+1}. Let U be a center potential defined as $U(x_i, y_i) = \frac{k}{2}((x_i - L))^2 + y_i^2)$ where the center is at point $(x, y) = (L, 0)$. In polar coordinates this becomes $U(r_i, \theta_i) = \frac{k}{2}(r_i^2 + L^2 - 2Lr_i\cos(\theta_i))$. Since $r_i = 1$ for all i we get $U(\theta_i) = \frac{k}{2}(1 + L^2 - 2L\cos(\theta_i))$. Using this potential in (1.71) we get:

$$\theta_{i+1} = \theta_i + \arcsin\left(\sin(\theta_i - \theta_{i-1}) - \frac{h^2 kL}{m}\sin(\theta_i)\right) \tag{1.72}$$

For the case of the potential centered at the origin, *i.e.* $L = 0$, (1.72) becomes:

$$\theta_{i+1} = 2\theta_i - \theta_{i-1} \tag{1.73}$$

As stated earlier, we can see that the step size h disappears from the equation. However, this is acceptable since the exact solution, (1.65), shows that for the central potential the particle moves with constant velocity. This is exactly the case in (1.73) as well. Therefore, this variational scheme will perfectly conserve energy for the origin-centered potential. Let's look at the exact solution for the off-origin center potential to see how (1.72) should behave.

We will use the Lagrangian in (1.63) except now the potential is defined as $U(r,\theta) = \frac{k}{2}\left(r^2 + L^2 - 2Lr\cos(\theta)\right)$. Applying the Euler-Lagrange equation for coordinate θ we get the equation of motion:

$$m\ddot{\theta} + \frac{\partial U}{\partial \theta} = 0 \tag{1.74}$$

$$m\ddot{\theta} + kL\sin(\theta) = 0 \tag{1.75}$$

This is exactly the same as the equation of motion for a simple pendulum, so we should expect a periodic solution. This variational scheme is first order accurate in h since the approximation of the velocity is first order accurate. We used a finite difference method for the velocity which can be derived using a Taylor series expansion.

$$f(x+h) = f(x) + hf'(x) + \frac{h^2 f''(x)}{2!} + \cdots \tag{1.76}$$

$$\frac{f(x+h)}{h} = \frac{f(x)}{h} + f'(x) + \frac{hf''(x)}{2!} \tag{1.77}$$

$$f'(x) = \frac{f(x+h) - f(x)}{h} - \frac{hf''(x)}{2!} \tag{1.78}$$

$$f'(x) = \frac{f(x+h) - f(x)}{h} + \mathcal{O}(h) \tag{1.79}$$

We can now see that the local truncation error is directly proportional to step size h. Comparing this to the other 2 numerical methods we investigated, the local truncation error for the forward Euler method is $\mathcal{O}(h^2)$ and the Runge-Kutta method is $\mathcal{O}(h^5)$.

Now we will compare the trajectories of these 3 schemes for the origin-centered potential, $L = 0$, with $m = 1$ and $k = 1$. As seen in Figure 1.3, the Euler method trajectory quickly explodes away from the unit circle, here we used stepsize $h = 0.1$. This graph shows the trajectory after 58 time steps.

For the Runge-Kutta method and our variational integrator in Figure 1.4, a stepsize of $h = 0.5$ was used. These trajectories are taken after 20000 timesteps. The Runge-Kutta method deviates from the constraint of the the unit circle, while the variational integrator stays close to the circle. This level of precision can be achieved with the RK4 method but at the cost of a decreased stepsize which means an increased number of computations if we

Figure 1.3 Numerically computed trajectory using an Euler method of a particle in an origin centered potential constrained to the unit circle with the starting position at $(x_0, y_0) = (1, 0)$.

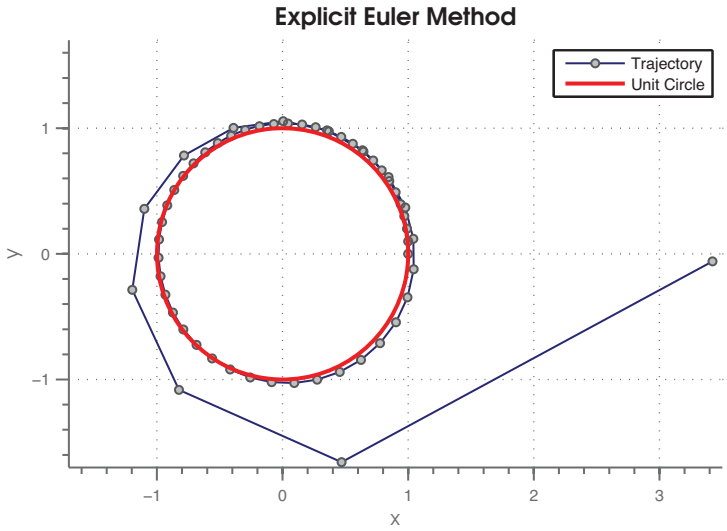

want the simulation to cover the same time interval. Comparing the energy of the two methods in Figure 1.5 we can see how the variational integrator conserves energy over long time intervals. This is due to the symplectic nature of variational integrators. The energy in the RK4 method on the other hand begins to oscillate with increasing amplitude as time increases. It also drifts and doesn't oscillate around a fixed center.

Now, let us look at the case with the off-center potential. For this case we set $L = 1$. Figure 1.6 shows the results. We can see that the trajectory is oscillating in the positive x hemisphere. This is an expected result as the exact solution to this problem showed that it should behave like a pendulum. Turning our attention to the total energy in Figure 1.6b we can see the symplectic nature of this integrator. Although the total energy oscillates, it does not drift or increase in amplitude like the Runge-Kutta method did. The rolling average was taken with a window size of 100 timesteps. One can see how the rolling average is constant and does not drift.

Conclusion

In conclusion, we have shown that variational integrators are effective for long-term simulations, including systems with holonomic constraints. This is because the total energy and momentum of the system is conserved over long time periods due to the symplectic nature of variational integrators. Variational integrators were compared to other well-known

numerical methods such as the Euler method and the 4th order Runge-Kutta method. These schemes were shown to not conserve energy over long time spans.

Figure 1.4 Numerically computed trajectory of a particle in an origin centered potential constrained to the unit circle. Comparing the numerical schemes of a fourth-order Runge-Kutta method and a variational integrator.

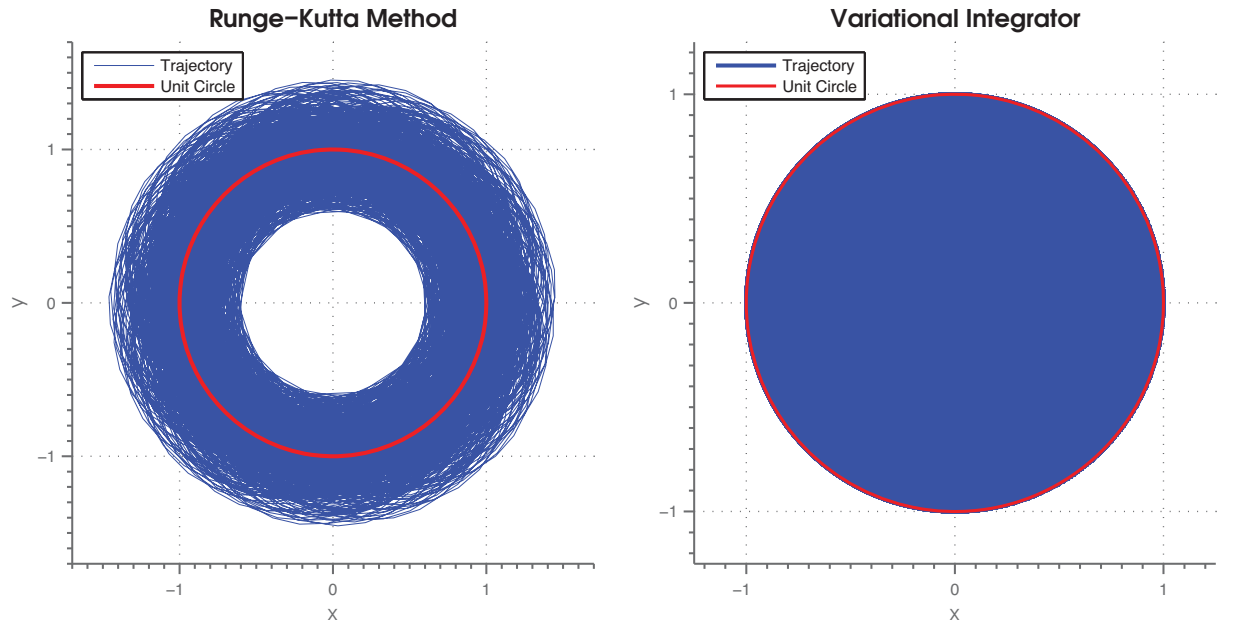

(a) Trajectory of RK4 method.

(b) Trajectory of variational integrator.

Figure 1.5 Total energy of a numerically computed particle in an origin centered potential constrained to the unit circle, comparing an RK4 method to a variational integrator.

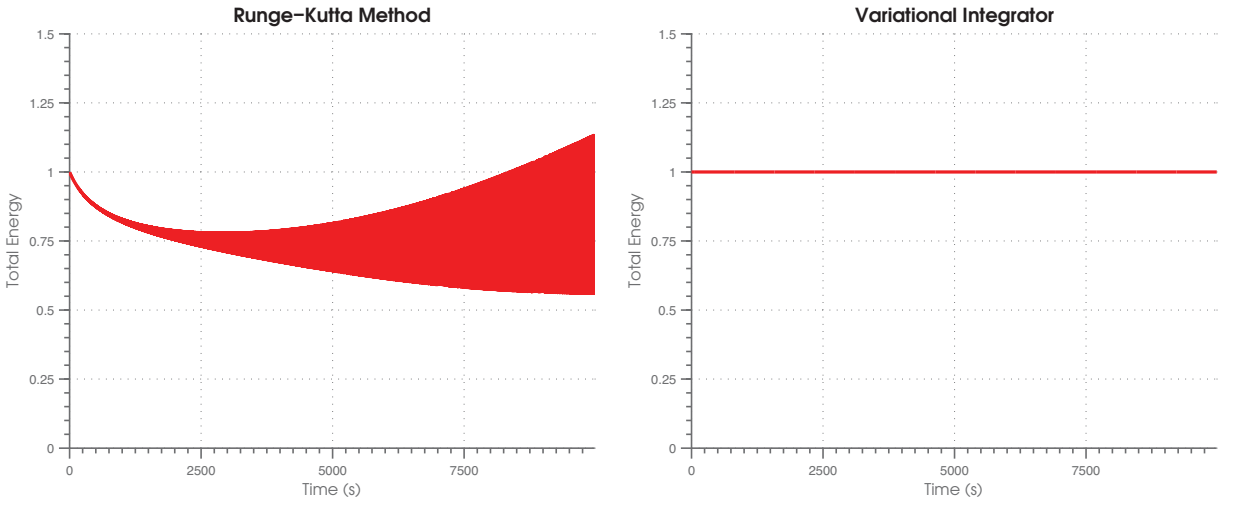

(a) Total energy of RK4 method.

(b) Total energy of variational integrator.

Figure 1.6 Numerically computed trajectory and total energy of a particle constrained to a unit circle in a center potential with center $(x, y) = (1, 0)$.

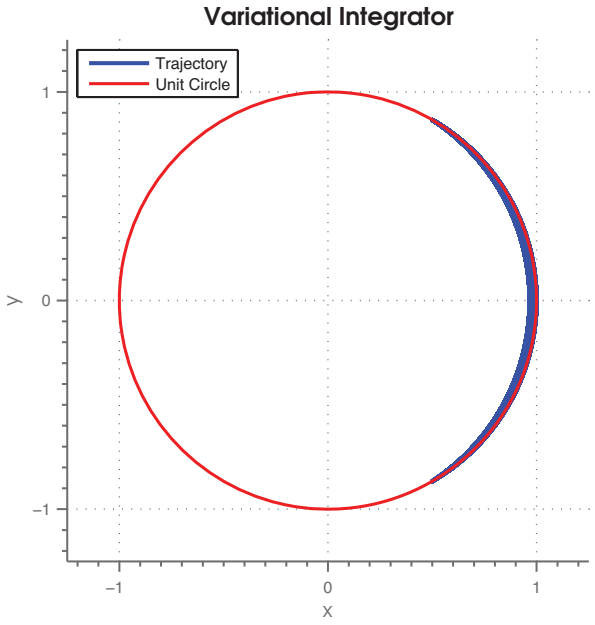

(a) Trajectory of variational integrator.

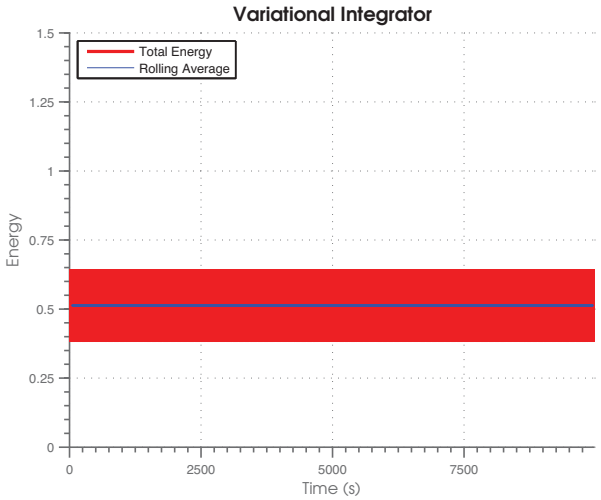

(b) Total energy and its rolling average of the variational integrator.

2 Variational Derivation of Garden Hose Model

In this section, we will review the variational integrator formulation of a garden hose model for discrete space and continuous time outlined in [7].

2.1 Fluid-conveying Tube with Dynamic Cross-sectional Area

First, we follow [5,6] which provides the basis to the variational derivation in the continuous case and takes into consideration the change in the cross-sectional area of the tube as it deforms. The dynamics of the tube are described using the geometric exact rod theory in [19]. The position of the tube of length L in 3-dimensional space is defined by 2 properties. First, the position of the geometric center or center of mass of the tube using the map $(s,t) \mapsto \mathbf{r}(s,t)$, where $s \in [0,L]$ and t is time. Second, the orientation of the cross sections of the tube at the points $\mathbf{r}(s,t)$ are defined by the moving orthonormal basis $\mathbf{e}_i(s,t) = \Lambda(s,t)\,\mathbf{E}_i$, $i = 1,2,3$, where $\Lambda(s,t) \in SO(3)$ and $\mathbf{E}_i$ is the fixed frame of reference. $SO(3)$ is also known as the special orthogonal matrix group or 3D rotation group, and is the set of square matrices with orthonormal columns and determinant 1.

Let the fluid passing through the tube be inviscid and incompressible. We define the position of the fluid particles, using the Lagrangian description of the fluid, by the one-dimensional mapping:

$$s = \phi(a,t) \tag{2.1}$$

a is the initial position, or original label, of the fluid particle and s is the position of the fluid particle located at $\mathbf{r}(s,t)$ at time t. We define the inverse of this mapping as the back-to-label map:

$$\psi(s,t) := \phi^{-1}(s,t) = a \tag{2.2}$$

Therefore, using the Eulerian description of fluid flow, the fluid moves with velocity relative to the tube:

$$u(s,t) = \phi_t \circ \phi^{-1} = \partial_t \phi(\psi(s,t),t), \quad s \in [0,L] \tag{2.3}$$

The centreline of the tube has velocity $\mathbf{v}_r = \partial_t \mathbf{r}$ and the fluid has velocity $\mathbf{v}_f = \partial_t \mathbf{r} + u\partial_s \mathbf{r}$. Therefore, the physical variables defining the motion of the tube in the tube's frame are the

local angular velocity, $\boldsymbol{\omega}$, and the local linear velocity $\boldsymbol{\gamma}$:

$$\boldsymbol{\omega} = \Lambda^{-1}\partial_t \Lambda \tag{2.4}$$

$$\boldsymbol{\gamma} = \Lambda^{-1}\partial_t \mathbf{r} \tag{2.5}$$

We also get the angular deformation or strain, $\boldsymbol{\Omega}$, and linear deformation, $\boldsymbol{\Gamma}$:

$$\boldsymbol{\Omega} = \Lambda^{-1}\partial_s \Lambda \tag{2.6}$$

$$\boldsymbol{\Gamma} = \Lambda^{-1}\partial_s \mathbf{r} \tag{2.7}$$

We now consider the changing cross sectional area of the tube. Let $A(s) = A(\boldsymbol{\Omega}(s), \boldsymbol{\Gamma}(s))$ define the cross sectional area of the tube at point $\mathbf{r}(s)$. As the tube bends or twists and changes area, the local frame rotates hence the dependence on $\boldsymbol{\Omega}$. Also, when the tube stretches and compresses the cross sectional area decreases and increases respectively, so the dependence on $\boldsymbol{\Gamma}$ is justified.

The amount of fluid entering the tube must equal the amount leaving the system for continuity. We constrain the system so that the fluid completely fills the space inside the tube. In order to formulate this constraint, we first must define the initial cross-sectional area $Q_0(a) := A_0(a)|\boldsymbol{\Gamma}(a)|$ where $|\boldsymbol{\Gamma}|$ takes into account that s does not necessarily define the arclength of the tube. If we assume the fluid is incompressible, we get the quantity $(Q_0 \circ \phi^{-1})\,\partial_s \phi^{-1}$ which we call the mass density. Therefore, we get the constraint:

$$Q_0(\psi(s,t))\,\partial_s \psi(s,t) = A(\boldsymbol{\Omega}, \boldsymbol{\Gamma})|\boldsymbol{\Gamma}| := Q(\boldsymbol{\Omega}, \boldsymbol{\Gamma}) \tag{2.8}$$

Differentiating the above with respect to time leads to the continuity equation or fluid volume conservation law:

$$\partial_t Q + \partial_s(Qu) = 0 \tag{2.9}$$

The Lagrangian used is derived in [6] and is as follows:

$$\ell = \frac{1}{2}\int \left(\alpha|\boldsymbol{\Gamma}|^2 + \langle \mathbb{I}\boldsymbol{\omega}, \boldsymbol{\omega}\rangle + \rho A(\boldsymbol{\Omega}, \boldsymbol{\Gamma})|\boldsymbol{\gamma} + \boldsymbol{\Gamma}u|^2 - \langle \mathbb{J}\boldsymbol{\Omega}, \boldsymbol{\Omega}\rangle - \lambda|\boldsymbol{\Gamma} - \boldsymbol{\chi}|^2\right)|\boldsymbol{\Gamma}|\,\mathrm{d}s \tag{2.10}$$

where α is the linear density of the tube, $\mathbb{I}$ is the local moment of inertia, ρ is the fluid density, $\mathbb{J}$ is the linear elasticity tensor, λ is the coefficient of stretch and let $\boldsymbol{\chi} = \mathbf{E}_3$ where

$\boldsymbol{\chi}$ is a fixed vector that points along the axis of the tube. The first 2 terms in the equation correspond to the kinetic energy of the tube, the third term corresponds to the kinetic energy of the fluid, and the last 2 terms come from the elastic potential energy of the tube.

The equations of motion are derived using a critical action principle where the constraint in (2.8) is enforced using Lagrange multiplier μ:

$$\delta \iint \left[\ell\left(\boldsymbol{\omega}, \boldsymbol{\gamma}, \boldsymbol{\Omega}, \boldsymbol{\Gamma}, u\right) - \mu\left(Q\left(\boldsymbol{\Omega}, \boldsymbol{\Gamma}\right) - Q_0\left(\psi\right)\partial_s \psi\right)\right] \mathrm{d}t\mathrm{d}s = 0 \tag{2.11}$$

The variations can be computed as:

$$\delta\boldsymbol{\omega} = \partial_t \boldsymbol{\Sigma} + \boldsymbol{\omega} \times \boldsymbol{\Sigma} \tag{2.12}$$

$$\delta\boldsymbol{\Omega} = \partial_s \boldsymbol{\Sigma} + \boldsymbol{\Omega} \times \boldsymbol{\Sigma} \tag{2.13}$$

$$\delta\boldsymbol{\gamma} = \partial_t \boldsymbol{\Psi} + \boldsymbol{\gamma} \times \boldsymbol{\Sigma} + \boldsymbol{\omega} \times \boldsymbol{\Psi} \tag{2.14}$$

$$\delta\boldsymbol{\Gamma} = \partial_s \boldsymbol{\Psi} + \boldsymbol{\Gamma} \times \boldsymbol{\Sigma} + \boldsymbol{\Omega} \times \boldsymbol{\Psi} \tag{2.15}$$

$$\delta u = \partial_t \eta + u\partial_s \eta - \eta \partial_s u \tag{2.16}$$

Where:

$$\boldsymbol{\Sigma} = \Lambda^{-1}\delta\Lambda, \quad \boldsymbol{\Psi} = \Lambda^{-1}\delta\mathbf{r}, \quad \eta = \delta\phi \circ \phi^{-1} \tag{2.17}$$

The variation of the first term of the critical action principle in (2.11) is defined as:

$$\iint \left[\left\langle \frac{\delta\ell}{\delta\boldsymbol{\omega}}, \delta\boldsymbol{\omega} \right\rangle + \left\langle \frac{\delta\ell}{\delta\boldsymbol{\gamma}}, \delta\boldsymbol{\gamma} \right\rangle + \left\langle \frac{\delta\ell}{\delta\boldsymbol{\Omega}}, \delta\boldsymbol{\Omega} \right\rangle + \left\langle \frac{\delta\ell}{\delta\boldsymbol{\Gamma}}, \delta\boldsymbol{\Gamma} \right\rangle + \left\langle \frac{\delta\ell}{\delta u}, \delta u \right\rangle\right] \mathrm{d}t\mathrm{d}s = 0 \tag{2.18}$$

Using integration by parts we get the variations in $\boldsymbol{\omega}$ and $\boldsymbol{\Omega}$:

$$\begin{aligned} \left\langle \frac{\delta\ell}{\delta\boldsymbol{\omega}}, \delta\boldsymbol{\omega} \right\rangle &= \left\langle \frac{\delta\ell}{\delta\boldsymbol{\omega}}, \partial_t \boldsymbol{\Sigma} + \boldsymbol{\omega} \times \boldsymbol{\Sigma} \right\rangle \\ &= \left\langle \partial_t \frac{\delta\ell}{\delta\boldsymbol{\omega}} + \boldsymbol{\omega} \times \frac{\delta\ell}{\delta\boldsymbol{\omega}}, \boldsymbol{\Sigma} \right\rangle \end{aligned} \tag{2.19}$$

$$\begin{aligned} \left\langle \frac{\delta\ell}{\delta\boldsymbol{\Omega}}, \delta\boldsymbol{\Omega} \right\rangle &= \left\langle \frac{\delta\ell}{\delta\boldsymbol{\Omega}}, \partial_s \boldsymbol{\Sigma} + \boldsymbol{\Omega} \times \boldsymbol{\Sigma} \right\rangle \\ &= \left\langle \partial_s \frac{\delta\ell}{\delta\boldsymbol{\Omega}} + \boldsymbol{\Omega} \times \frac{\delta\ell}{\delta\boldsymbol{\Omega}}, \boldsymbol{\Sigma} \right\rangle \end{aligned} \tag{2.20}$$

The variations in $\boldsymbol{\gamma}$ and $\boldsymbol{\Gamma}$ are:

$$\begin{aligned} \left\langle \frac{\delta\ell}{\delta\boldsymbol{\gamma}}, \delta\boldsymbol{\gamma} \right\rangle &= \left\langle \frac{\delta\ell}{\delta\boldsymbol{\gamma}}, \partial_t \boldsymbol{\Psi} + \boldsymbol{\gamma} \times \boldsymbol{\Sigma} + \boldsymbol{\omega} \times \boldsymbol{\Psi} \right\rangle \\ &= \left\langle \boldsymbol{\gamma} \times \frac{\delta\ell}{\delta\boldsymbol{\gamma}}, \boldsymbol{\Sigma} \right\rangle + \left\langle \partial_t \frac{\delta\ell}{\delta\boldsymbol{\gamma}} + \boldsymbol{\omega} \times \frac{\delta\ell}{\delta\boldsymbol{\gamma}}, \boldsymbol{\Psi} \right\rangle \end{aligned} \tag{2.21}$$

$$\begin{aligned}\left\langle \frac{\delta \ell}{\delta \mathbf{\Gamma}}, \delta \mathbf{\Gamma} \right\rangle &= \left\langle \frac{\delta \ell}{\delta \mathbf{\Gamma}}, \partial_s \mathbf{\Psi} + \mathbf{\Gamma} \times \mathbf{\Sigma} + \mathbf{\Omega} \times \mathbf{\Psi} \right\rangle \\ &= \left\langle \mathbf{\Gamma} \times \frac{\delta \ell}{\delta \mathbf{\Gamma}}, \mathbf{\Sigma} \right\rangle + \left\langle \partial_s \frac{\delta \ell}{\delta \mathbf{\Gamma}} + \mathbf{\Omega} \times \frac{\delta \ell}{\delta \mathbf{\Gamma}}, \mathbf{\Psi} \right\rangle\end{aligned} \tag{2.22}$$

The variation in u is:

$$\begin{aligned}\left\langle \frac{\delta \ell}{\delta u}, \delta u \right\rangle &= \left\langle \frac{\delta \ell}{\delta u}, \partial_t \eta + u \partial_s \eta - \eta \partial_s u \right\rangle \\ &= \left\langle \partial_t \frac{\delta \ell}{\delta u} + u \partial_s \frac{\delta \ell}{\delta u} + \frac{\delta \ell}{\delta u} \partial_s u, \eta \right\rangle\end{aligned} \tag{2.23}$$

We now have variations of the first term, variations of the second term can be written as:

$$\begin{aligned}&\delta \iint \mu \left(Q \left(\mathbf{\Omega}, \mathbf{\Gamma} \right) - Q_0 \left(\psi \right) \partial_s \psi \right) \mathrm{d}t\mathrm{d}s \\ &= \iint \Bigg[\delta \mu \left(Q \left(\mathbf{\Omega}, \mathbf{\Gamma} \right) - Q_0 \left(\psi \right) \partial_s \psi \right) + \mu \frac{\partial Q}{\partial \mathbf{\Omega}} \cdot \delta \mathbf{\Omega} + \mu \frac{\partial Q}{\partial \mathbf{\Gamma}} \cdot \delta \mathbf{\Gamma} + \\ &\quad + \mu \partial_s \left(Q_0 \left(\psi \right) \partial_s \psi \right) \left(\delta \phi \left(\psi \right) \right) \Bigg] \mathrm{d}t\mathrm{d}s \\ &= \iint \Bigg[\delta \mu \left(Q \left(\mathbf{\Omega}, \mathbf{\Gamma} \right) - Q_0 \left(\psi \right) \partial_s \psi \right) - \left(\left(\partial_s + \mathbf{\Omega} \times \right) \mu \frac{\partial Q}{\partial \mathbf{\Omega}} + \mathbf{\Gamma} \times \mu \frac{\partial Q}{\partial \mathbf{\Gamma}} \right) \cdot \mathbf{\Sigma} \\ &\quad - \left(\partial_s + \mathbf{\Omega} \times \right) \mu \frac{\partial Q}{\partial \mathbf{\Gamma}} \cdot \mathbf{\Psi} - Q \partial_s \mu \eta \Bigg] \mathrm{d}t\mathrm{d}s\end{aligned} \tag{2.24}$$

We have now computed all the variations. If we collect terms proportional to $\mathbf{\Sigma}$, $\mathbf{\Psi}$, and η, we get the conservation law for angular momentum, linear momentum, and fluid momentum respectively:

$$\left(\partial_t + \boldsymbol{\omega} \times \right) \frac{\delta \ell}{\delta \boldsymbol{\omega}} + \boldsymbol{\gamma} \times \frac{\delta \ell}{\delta \boldsymbol{\gamma}} + \left(\partial_s + \mathbf{\Omega} \times \right) \left(\frac{\delta \ell}{\delta \mathbf{\Omega}} - \mu \frac{\partial Q}{\partial \mathbf{\Omega}} \right) + \mathbf{\Gamma} \times \left(\frac{\delta \ell}{\delta \mathbf{\Gamma}} - \mu \frac{\partial Q}{\partial \mathbf{\Gamma}} \right) = 0 \tag{2.25}$$

$$\left(\partial_t + \boldsymbol{\omega} \times \right) \frac{\delta \ell}{\delta \boldsymbol{\gamma}} + \left(\partial_s + \mathbf{\Omega} \times \right) \left(\frac{\delta \ell}{\delta \mathbf{\Gamma}} - \mu \frac{\partial Q}{\partial \mathbf{\Gamma}} \right) = 0 \tag{2.26}$$

$$\partial_t m + \partial_s \left(m u - \mu \right) = 0, \quad m = \frac{1}{Q} \frac{\partial \ell}{\partial u} \tag{2.27}$$

2.2 Spatial Discretization

We can now discretize the previous variational system in space but leave time continuous. Here we review the framework laid out in [7]. Let the distance between space steps be

constant $s_{i+1} - s_i = h$. We discretize the angular strain, $\mathbf{\Omega}$, and linear strain, $\mathbf{\Gamma}$, by:

$$\lambda_i = \Lambda_i^{-1} \Lambda_{i+1} \tag{2.28}$$

$$\boldsymbol{\kappa}_i = \Lambda_i^{-1} \left(\mathbf{r}_{i+1} - \mathbf{r}_i \right) \tag{2.29}$$

The local linear and angular velocities are discretized as:

$$\boldsymbol{\omega}_i = \Lambda_i^{-1} \dot{\Lambda}_i \tag{2.30}$$

$$\boldsymbol{\gamma}_i = \Lambda_i^{-1} \dot{\boldsymbol{r}}_i \tag{2.31}$$

Next, we must formulate a discretization for the fluid velocity $u_i = u\left(s_i, t\right)$ by discretizing the back-to-labels map $\psi\left(s,t\right) := \phi^{-1}\left(s,t\right) = a$. Now, I discretize $\psi_i := \psi\left(s_i, t\right)$ using linear interpolation between s_i and s_{i+1}.

$$\psi\left(s,t\right) = \psi_i + \frac{s - s_i}{s_{i+1} - s_i} \left(\psi_{i+1} - \psi_i \right) = a, \quad s_i < s < s_{i+1} \tag{2.32}$$

Inverting the above equation leads to the Lagrangian mapping:

$$\phi\left(a,t\right) = s_i + \frac{a - \psi_i}{\psi_{i+1} - \psi_i} \left(s_{i+1} - s_i \right) = s, \quad a_i < a < a_{i+1} \tag{2.33}$$

This inversion works if a stays between ψ_i and ψ_{i+1}, which holds true if the step size is sufficiently small enough. The linear interpolation is simple to invert, however, higher order interpolation is also possible. Next, we compute the Eulerian fluid velocity in (2.3):

$$u\left(s,t\right) = \phi_t \circ \psi = \partial_t \phi\left(\psi\left(s,t\right), t\right) = -\frac{\left(s - s_i\right)\left(\dot{\psi}_{i+1} - \dot{\psi}_i\right) + \left(s_{i+1} - s_i\right)\dot{\psi}_i}{\psi_{i+1} - \psi_i} \tag{2.34}$$

Leading to the discrete relative fluid velocity:

$$u_i = -\frac{s_{i+1} - s_i}{\psi_{i+1} - \psi_i} \dot{\psi}_i \tag{2.35}$$

We now turn our attention to discretizing the constraint in (2.8). For simplification, one makes the assumption that the tube is straight and the cross-sectional area is constant when the tube is at rest, in other words Q_0 is constant. Substituting (2.32) into (2.8), we get the discrete constraint:

$$Q_0 \frac{\psi_{i+1} - \psi_i}{s_{i+1} - s_i} = F\left(\lambda_i, \boldsymbol{\kappa}_i\right) := F_i \tag{2.36}$$

Differentiating the above equation with respect to time and using $s_{i+1} - s_i = h$ we get:

$$\dot{\psi}_{i+1} - \dot{\psi}_i = \frac{\mathrm{d}}{\mathrm{d}t}\frac{h}{Q_0}F_i \tag{2.37}$$

From (2.35) and (2.36) the following holds true:

$$\dot{\psi}_i = -\frac{F_i}{Q_0}u_i \tag{2.38}$$

Therefore, using (2.37) and (2.38), the discrete fluid conservation law can be written as:

$$\frac{\mathrm{d}}{\mathrm{d}t}\left(hF_i\right) + F_{i+1}u_{i+1} - F_i u_i = 0 \tag{2.39}$$

In the following sections, we utilize the above discretization with linear interpolation. However, we can still formulate a more general discretization of the fluid without linear interpolation. One must first rewrite the relative fluid velocity in terms of the back-to-labels map:

$$u\left(s,t\right) = \partial_t\phi \circ \psi\left(s,t\right) = -\frac{\partial_t\psi\left(s,t\right)}{\partial_s\psi\left(s,t\right)} \tag{2.40}$$

Define the discretization of the derivative $\partial_s\psi\left(s_i,t\right)$ using the linear operator D_i acting on the vector $\overline{\psi} = \left(\psi_1, \psi_2, \ldots, \psi_n\right)$:

$$D_i\overline{\psi}\left(t\right) := \sum_{j\in J} a_j\psi_{i+j}\left(t\right) \tag{2.41}$$

Where J is a finite set of integers in some neighbourhood of $j = 0$. For the linear interpolation case:

$$D_i\overline{\psi} = \frac{\psi_{i+1} - \psi_i}{s_{i+1} - s_i} \tag{2.42}$$

The fluid velocity is then discretized by:

$$u_i = -\frac{\dot{\psi}_i}{D_i\overline{\psi}} \tag{2.43}$$

and the fluid constraint becomes:

$$Q_0 D_i\overline{\psi} = F\left(\lambda_i, \boldsymbol{\kappa}_i\right) := F_i \tag{2.44}$$

Differentiating the above equation with respect to time and using (2.43) we get the conservation law:

$$\dot{F}_i + D_i\left(\overline{uF}\right) = 0 \tag{2.45}$$

Now, using the above discretizations and the continuous Lagrangian in (2.10), the discrete Lagrangian reads:

$$\ell = \sum_i \frac{1}{2}\left(\alpha\left|\boldsymbol{\gamma}_i\right|^2 + \langle \mathbb{I}\boldsymbol{\omega}_i, \boldsymbol{\omega}_i\rangle + \rho F(\boldsymbol{\kappa}_i, \lambda_i)\left|\boldsymbol{\gamma}_i + \frac{\boldsymbol{\kappa}_i}{h}u_i\right|^2 - \langle \mathbb{J}\lambda_i, \lambda_i\rangle - \xi\left|\frac{\boldsymbol{\kappa}_i}{h} - \boldsymbol{\chi}\right|^2\right)\left|\frac{\boldsymbol{\kappa}_i}{h}\right| \tag{2.46}$$

We now impose the critical action principle to find the equations of motions:

$$\delta\int\sum_i\left[\ell\left(\boldsymbol{\gamma}_i, \boldsymbol{\omega}_i, \boldsymbol{\kappa}_i, \lambda_i, u_i\right) + \mu_i\left(Q_0 D_i\bar{\psi} - F\left(\lambda_i, \boldsymbol{\kappa}_i\right)\right)\right]\mathrm{d}t = 0 \tag{2.47}$$

Here the Lagrange multiplier μ_i enforces the holonomic constraint of the fluid completely filling the interior of the tube. Computing the variations we arrive at the discrete conservation law for linear momentum,

$$\left(\frac{d}{dt} + \boldsymbol{\omega}_i\times\right)\frac{\delta\ell}{\delta\boldsymbol{\gamma}_i} + \left(\frac{\delta\ell}{\delta\boldsymbol{\kappa}_i} - \mu_i\frac{\partial F}{\partial\boldsymbol{\kappa}_i}\right) - \lambda_{i-1}^T\left(\frac{\delta\ell}{\delta\boldsymbol{\kappa}_{i-1}} - \mu_{i-1}\frac{\partial F}{\partial\boldsymbol{\kappa}_{i-1}}\right) = \mathbf{0} \tag{2.48}$$

the discrete conservation law for angular momentum,

$$\begin{aligned}\left(\frac{d}{dt} + \boldsymbol{\omega}_i\times\right)\frac{\delta\ell}{\delta\boldsymbol{\omega}_i} + \boldsymbol{\gamma}_i\times\frac{\delta\ell}{\delta\boldsymbol{\gamma}_i} + \left[\left(\frac{\partial\ell}{\partial\lambda_i} - \mu_i\frac{\partial F}{\partial\lambda_i}\right)\lambda_i^T - \lambda_{i-1}^T\left(\frac{\partial\ell}{\partial\lambda_{i-1}} - \mu_{i-1}\frac{\partial F}{\partial\lambda_{i-1}}\right)\right]^\vee \\ + \boldsymbol{\kappa}_i\times\left(\frac{\partial\ell}{\partial\boldsymbol{\kappa}_i} - \mu_i\frac{\partial F}{\partial\boldsymbol{\kappa}_i}\right) = \mathbf{0}\end{aligned} \tag{2.49}$$

and the discrete conservation law for fluid momentum:

$$\frac{\mathrm{d}}{\mathrm{d}t}\left(\frac{1}{F_i}\frac{\delta\ell}{\delta u_i}\right) + \frac{1}{h}\left(\frac{u_i}{F_i}\frac{\delta\ell}{\delta u_i} - \frac{u_{i-1}}{F_{i-1}}\frac{\delta\ell}{\delta u_{i-1}} + \mu_i - \mu_{i-1}\right) = 0 \tag{2.50}$$

Along with (2.39), these equations form the discrete analogs of the continuous conservation laws in (2.9), (2.25), (2.26), and (2.27). The terms proportional to μ_i utilize the dynamically changing cross sectional area property.

Conclusion

In conclusion, in this section we laid out the variational formulation of a fluid-conveying tube with dynamic cross-sectional area. This was achieved in both the continuous case as well as in the case with discrete space but continuous time. In the following section, we will make use of the spatial discretization derived above. More specifically we will utilize the discrete linear momentum conservation law as well as the discrete fluid volume conservation law (2.39).

3 Discretization of a 1-Dimensional Stretching Tube

The main result of the thesis lies in this section and it contains new material. Using the variational method derived in the previous section, we will create a simple model of the tube and study the ordinary differential equations it produces. For ease of calculations, let the tube be constrained to motion in one dimension with no rotation. This is equivalent to a tube being stretched and compressed along the length of the tube. First, we discretize the tube using 3 points and find the equation of motion analytically. Next, we study the linear stability of the resulting ODE. Last, we provide a discretization using N-points.

3.1 3 - Point Discretization

Let us discretize the tube into 3 points. The first point is fixed in place while the second point stretches away from the first point. The last point has free end conditions so we let it stay a fixed distance away from the second point. The first step is to form the discrete Lagrangian:

$$\ell = \sum_i \frac{1}{2}\left(\alpha\left|\boldsymbol{\gamma}_i\right|^2 + \langle \mathbb{I}\boldsymbol{\omega}_i, \boldsymbol{\omega}_i\rangle + \rho F(\boldsymbol{\kappa}_i, \lambda_i)\left|\boldsymbol{\gamma}_i + \frac{\boldsymbol{\kappa}_i}{h}u_i\right|^2 - \langle \mathbb{J}\lambda_i, \lambda_i\rangle - \xi\left|\frac{\boldsymbol{\kappa}_i}{h} - \boldsymbol{\chi}\right|^2\right)\left|\frac{\boldsymbol{\kappa}_i}{h}\right| \tag{3.1}$$

$$\ell = \sum_i \mathcal{L}_i\left|\frac{\boldsymbol{\kappa}_i}{h}\right| \tag{3.2}$$

Where:

$$\boldsymbol{\kappa}_i = \Lambda_i^{-1}\left(\boldsymbol{r}_{i+1} - \boldsymbol{r}_i\right) \tag{3.3}$$

$$\lambda_i = \Lambda_i^{-1}\Lambda_{i+1} \tag{3.4}$$

$$\boldsymbol{\omega}_i = \Lambda_i^{-1}\dot{\Lambda}_i \tag{3.5}$$

$$\boldsymbol{\gamma}_i = \Lambda_i^{-1}\dot{\boldsymbol{r}}_i \tag{3.6}$$

Now let us define the variables. Since this tube only moves in the E_1 direction it will have no rotation. So we define the local frame Λ_i as:

$$\Lambda_0 = \Lambda_1 = \Lambda_2 = Id \tag{3.7}$$

The subscript indicates the corresponding point along the tube. Since we restricted the system to one dimension, the vectors defined above are now scalars. The position of the points along the tube are as follows:

$$\begin{aligned} r_0 &= 0 \\ r_1 &= h + hx \\ r_2 &= 2h + hx \end{aligned} \tag{3.8}$$

The rest of the variables follow from the above set-up:

$$\kappa_0 = h + hx, \quad \kappa_1 = h \tag{3.9}$$

$$\lambda_0 = \lambda_1 = Id \tag{3.10}$$

$$\omega_0 = \omega_1 = \omega_2 = 0 \tag{3.11}$$

$$\gamma_0 = 0, \quad \gamma_1 = \gamma_2 = h\dot{x} \tag{3.12}$$

The cross sectional area of the tube is defined as:

$$F_i = F_a - \frac{\beta}{2} |\kappa_i - h|^2 \tag{3.13}$$

where F_a is the cross sectional area of the tube with no deformation. Therefore, we get:

$$F_0 = F_a - \frac{\beta}{2} h^2 x^2, \quad F_1 = F_a \tag{3.14}$$

The more the tube gets stretched, the smaller the cross sectional area becomes.

3.2 Conservation Laws

We can now create the equations of motion using the conservation laws derived above. Since the tube is restricted to motion in one dimension and it is not allowed to twist, the angular momentum equation has a trivial solution.

3.2.1 Fluid Volume

The discrete analogue of conservation of fluid volume defined by (2.39) is given by:

$$\frac{d}{dt}(hF_0) + F_1 u_1 - F_0 u_0 = 0 \tag{3.15}$$

We use the previous equation to solve for u_1 and $\dot{u_1}$ to close the system in the following derivation.

$$u_1 = u_0 \frac{F_0}{F_1} + \frac{\beta h^3 x \dot{x}}{F_1} \tag{3.16}$$

$$\dot{u_1} = \frac{\beta h^3 \left(\dot{x}^2 + x\ddot{x}\right)}{F_1} - \frac{\beta h^2 u_0 x \dot{x}}{F_1} \tag{3.17}$$

3.2.2 Linear Momentum

The discrete equivalent of the linear momentum conservation law is given by:

$$\left(\frac{d}{dt} + \boldsymbol{\omega}_i \times\right) \frac{\delta \ell}{\delta \boldsymbol{\gamma}_i} + \left(\frac{\delta \ell}{\delta \boldsymbol{\kappa}_i} - \mu_i \frac{\partial F}{\partial \boldsymbol{\kappa}_i}\right) - \lambda_{i-1}^T \left(\frac{\delta \ell}{\delta \boldsymbol{\kappa}_{i-1}} - \mu_{i-1} \frac{\partial F}{\partial \boldsymbol{\kappa}_{i-1}}\right) = \mathbf{0} \tag{3.18}$$

Since there are only 3 points in this simple system, we only have to look at the equation with $i = 1$. Also, since there is no rotation or twist, (3.18) can be simplified to:

$$\frac{d}{dt}\left(\frac{\delta \ell}{\delta \gamma_1}\right) + \frac{\delta \ell}{\delta \kappa_1} - \mu_1 \frac{\partial F_1}{\partial \kappa_1} - \frac{\delta \ell}{\delta \kappa_0} + \mu_0 \frac{\partial F_0}{\partial \kappa_0} = 0 \tag{3.19}$$

We begin by solving for the first term involving $\frac{\delta \ell}{\delta \boldsymbol{\gamma}_1}$:

$$\frac{\delta \ell}{\delta \gamma_i} = \left[\alpha \gamma_i + \rho F\left(\kappa_i, \lambda_i\right)\left(\gamma_i + \frac{\kappa_i}{h} u_i\right)\right] \left|\frac{\kappa_i}{h}\right| \tag{3.20}$$

$\left|\frac{\kappa_1}{h}\right| = 1$, so we get:

$$\frac{\delta \ell}{\delta \gamma_1} = \left(\alpha h + \rho F_1\right) \dot{x} + \rho F_1 u_1 \tag{3.21}$$

Therefore, the first term of (3.19) can be written as:

$$\begin{aligned} \frac{d}{dt}\left(\frac{\delta \ell}{\delta \gamma_1}\right) &= \left(\alpha h + \rho F_1 h\right) \ddot{x} + \rho \dot{F_1} h \dot{x} + \rho \dot{F_1} u_1 + \rho F_1 \dot{u_1} \\ &= \left(\alpha h + \rho F_1 h\right) \ddot{x} + \rho F_1 \dot{u_1} \end{aligned} \tag{3.22}$$

Where we used $\dot{F_1} = 0$. Next we solve for $\frac{\delta \ell}{\delta \kappa_i}$:

$$\frac{\delta \ell}{\delta \kappa_i} = \mathcal{L}_i \frac{\kappa_i}{h^2 \left|\frac{\kappa_i}{h}\right|} + \frac{\delta \mathcal{L}_i}{\delta \kappa_i} \left|\frac{\kappa_i}{h}\right| \tag{3.23}$$

We start by finding $\mathcal{L}_0$ and $\mathcal{L}_1$. :

$$\mathcal{L}_0 = \frac{1}{2}\left[\rho F_0 \left|\frac{\kappa_0 u_0}{h}\right|^2 - \operatorname{Tr} \mathbb{J} - \xi \left|\frac{\kappa_0}{h} - \boldsymbol{\chi}\right|^2\right] \tag{3.24}$$

$$\mathcal{L}_1 = \frac{1}{2}\left[\alpha \left|\gamma_1\right|^2 + \rho F_1 \left|\gamma_1 + \frac{\kappa_1 u_1}{h}\right|^2 - \operatorname{Tr} \mathbb{J} - \xi \left|\frac{\kappa_1}{h} - \boldsymbol{\chi}\right|^2\right] \tag{3.25}$$

$$\mathcal{L}_0 = \frac{1}{2}\left[\rho F_0 u_0^2 (1+x)^2 - \operatorname{Tr}\mathbb{J} - \xi x^2\right] \tag{3.26}$$

$$\mathcal{L}_1 = \frac{1}{2}\left[\alpha h^2 \dot{x}^2 + \rho F_1 (h\dot{x} + u_1)^2 - \operatorname{Tr}\mathbb{J}\right] \tag{3.27}$$

We then calculate $\frac{\delta \mathcal{L}_i}{\delta \boldsymbol{\kappa}_i}$:

$$\frac{\delta \mathcal{L}_i}{\delta \kappa_i} = \frac{\rho}{2}\frac{\partial F_i}{\partial \kappa_i}\left|\gamma_i + \frac{\kappa_i u_i}{h}\right|^2 + \frac{\rho F_i u_i}{h}\left(\gamma_i + \frac{\kappa_i u_i}{h}\right) - \frac{\xi}{h}\left(\frac{\kappa_i}{h} - \boldsymbol{\chi}\right) \tag{3.28}$$

Where we have:

$$\frac{\partial F_0}{\partial \kappa_0} = -\beta h x \tag{3.29}$$

$$\frac{\partial F_1}{\partial \kappa_1} = 0 \tag{3.30}$$

Therefore, we arrive at:

$$\frac{\delta \mathcal{L}_0}{\delta \kappa_0} = -\frac{1}{2}\rho\beta h u_0^2 x (1+x)^2 + \frac{\rho F_0 u_0^2}{h}(1+x) - \frac{\xi}{h}x \tag{3.31}$$

$$\frac{\delta \mathcal{L}_1}{\delta \kappa_1} = \frac{\rho F_1 u_1}{h}(h\dot{x} + u_1) \tag{3.32}$$

We can now put (3.31) and (3.32) back into (3.23), where we have $\left|\frac{\kappa_0}{h}\right| = 1 + x$, $\left|\frac{\kappa_1}{h}\right| = 1$, and $\mathcal{L}_0$, $\mathcal{L}_1$ are defined in (3.26) and (3.27) respectively.

$$\frac{\delta \ell}{\delta \kappa_0} = \frac{\mathcal{L}_0}{h} - \frac{1}{2}\rho\beta h u_0^2 x (1+x)^3 + \frac{\rho F_0 u_0^2}{h}(1+x)^2 - \frac{\xi}{h}x(1+x) \tag{3.33}$$

$$\frac{\delta \ell}{\delta \kappa_1} = \frac{\mathcal{L}_1}{h} + \frac{\rho F_1 u_1^2}{h} + \rho F_1 u_1 \dot{x} \tag{3.34}$$

All terms in the linear momentum conservation law, (3.19), have now been calculated, so using (3.22), (3.29), (3.30), (3.33) and (3.34), we get the equation of motion:

$$\begin{aligned}&(\alpha h + \rho F_1 h)\ddot{x} + \rho F_1 \dot{u}_1 + \frac{\mathcal{L}_1}{h} + \frac{\rho F_1 u_1^2}{h} + \rho F_1 u_1 \dot{x} \\ &- \left(\frac{\mathcal{L}_0}{h} - \frac{1}{2}\rho\beta h u_0^2 x (1+x)^3 + \frac{\rho F_0 u_0^2}{h}(1+x)^2 - \frac{\xi}{h}x(1+x)\right) - \mu_0 \beta h x = 0\end{aligned} \tag{3.35}$$

We would like this equation to be in terms of x, derivatives of x, and u_1, so we can expand the following term:

$$\begin{aligned}\frac{\mathcal{L}_1 - \mathcal{L}_0}{h} &= \frac{1}{2h}\left[\alpha h^2 \dot{x}^2 + \rho F_1 (h\dot{x} + u_1)^2 - \operatorname{Tr}\mathbb{J} - \left(\rho F_0 u_0^2 (1+x)^2 - \operatorname{Tr}\mathbb{J} - \xi x^2\right)\right] \\ &= \frac{1}{2h}\left[\alpha h^2 \dot{x}^2 + \rho F_1 h^2 \dot{x}^2 + 2\rho F_1 u_1 h \dot{x} + \rho F_1 u_1^2 - \rho F_0 u_0^2 (1+x)^2 + \xi x^2\right]\end{aligned} \tag{3.36}$$

Substituting (3.17) for $\dot{u}_1$ and using the above equation, the linear momentum conservation law can be written in terms of $x, \dot{x}, \ddot{x}$ and u_1:

$$\begin{aligned}&(\alpha h + \rho F_1 h)\,\ddot{x} + \rho\beta h^3 x\ddot{x} + \left(\rho\beta h^3 + \frac{1}{2}\alpha h + \frac{1}{2}\rho F_1 h\right)\dot{x}^2 - \rho\beta h^2 u_0 x\dot{x} + \\ &+ 2\rho F_1 u_1\dot{x} + \frac{3}{2}\frac{\rho F_1 u_1^2}{h} - \frac{3}{2}\frac{\rho F_0 u_0^2}{h}(1+x)^2 + \frac{3\xi x^2}{2h} + \frac{\xi x}{h} + \frac{1}{2}\rho\beta h u_0^2 x\,(1+x)^3 + \\ &- \mu_0\beta h x = 0\end{aligned} \tag{3.37}$$

Now we divide equation (3.37) by $\rho F_1 h$ and multiply by T^2, where $\tau = \frac{t}{T}$ and $(\quad)' = \frac{d}{d\tau}$, to get the simplified equation of motion for the 1-dimensional stretching tube:

$$\begin{aligned}&(A + 1 + \beta Z x)\,x'' + \left(\beta Z + \frac{1}{2}A + \frac{1}{2}\right)x'^2 - \beta Z V_0 x x' + 2V_1 x' + \frac{3}{2}V_1^2 + \\ &- \frac{3}{2}V_0^2\frac{F_0}{F_1}(1+x)^2 + \frac{3}{2}Px^2 + Px + \frac{1}{2}V_0^2\beta Z x\,(1+x)^3 - \frac{\mu_0\beta T^2}{\rho F_1}x = 0\end{aligned} \tag{3.38}$$

where:

$$A = \frac{\alpha}{\rho F_1}, Z = \frac{h^2}{F_1}, V_i = \frac{u_i T}{h}, P = \frac{\xi T^2}{\rho h^2 F_1}$$

The fluid volume conservation can be rewritten as:

$$V_1 = V_0\frac{F_0}{F_1} + \beta Z x x' \tag{3.39}$$

We can now solve (3.38) numerically in MATLAB and observe the behaviour of the 3 point stretching tube system. Figure 3.1 shows different trajectories as the initial velocity, x_0', is varied. The parameters used are:

$$h = 0.1,\ T = 1,\ \mu_0 = 1,\ \rho = 11,\ F_1 = 2,\ \alpha = 1,\ \beta = 3,\ \xi = 1,\ u_0 = 0.5 \tag{3.40}$$

It is clear that the system quickly stabilizes to 2 equilibria. We have 2 stable nodes around $x = 8$ and $x = -2.5$. We notice that there are a couple unstable equilibria as well. The solutions repel away from $x = 0$ and somewhere in $x < -5$ the solutions begin to explode.

Figure 3.1 Trajectories of the 1-dimensional stretching tube system, where $x(t)$ is the displacement of the center point from the resting position. The initial conditions are $x_0 = 0$ and x_0' varied from 10 to -25.

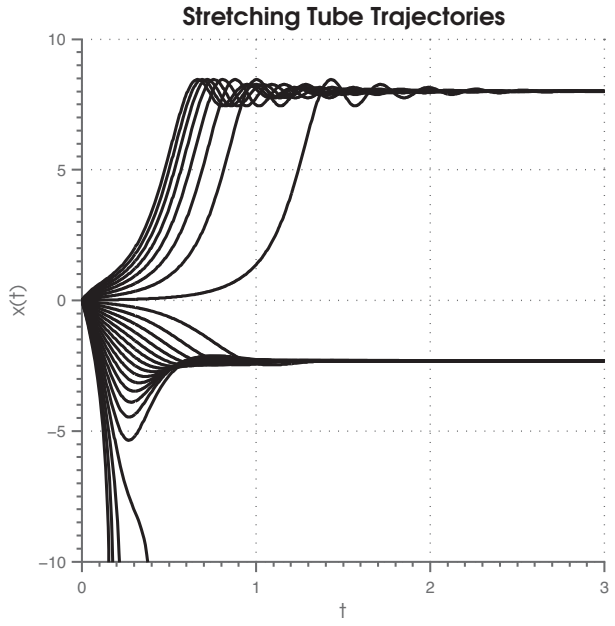

3.3 Stability Analysis

3.3.1 Steady State Solutions

Let us now analyse and study the stability of this system. First, we will look for steady state solutions. So let us write (3.38) with $x' = x'' = 0$

$$\frac{3}{2}V_0^2\left(\frac{F_0}{F_1}\right)^2 - \frac{3}{2}V_0^2\frac{F_0}{F_1}(1+x)^2 + P\left(\frac{3}{2}x^2 + x\right) + \frac{1}{2}V_0^2\beta Z x(1+x)^3 - \frac{\mu_0\beta T^2}{\rho F_1}x = 0 \quad (3.41)$$

Now, we want to find x_0 which is a solution of this steady state equation. So let us expand (3.41):

$$\frac{3}{2}V_0^2\left[\left(1-\frac{\beta Z x^2}{2}\right)^2 - \left(1-\frac{\beta Z x^2}{2}\right)(1+x)^2\right] + P\left(\frac{3}{2}x^2 + x\right) + \tilde{Z}x(1+x)^3 - M_0 x = 0 \quad (3.42)$$

$$\frac{3}{2}V_0^2\left[-\frac{\beta Z x^2}{2} + \frac{\beta^2 Z^2 x^4}{4} - 2x - x^2 + \frac{\beta Z x^2}{2}\left(2x + x^2\right)\right] + Px\left(\frac{3}{2}x + 1\right) + \tilde{Z}x(1+x)^3 - M_0 x = 0 \quad (3.43)$$

Figure 3.2 Real-valued equilibrium points of the 1-dimensional stretching tube as the fluid velocity, u_0, is increased from 0 to 2. $x = 0$ is an equilibrium point for all u_0.

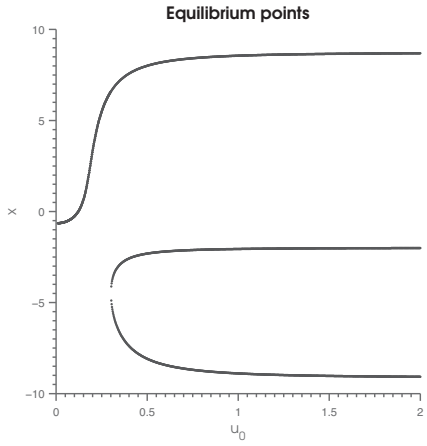

For simplification, let us take:

$$\tilde{Z} = \frac{1}{2}V_0^2 \beta Z, \quad M_0 = \frac{\mu_0 \beta T^2}{\rho F_1}$$

We can see that x is common to all terms in (3.43). Therefore, we know that one solution to the steady state equation is $x_0 = 0$.

$$x\left(\frac{3}{2}V_0^2\left[-\frac{\beta Z x}{2} + \frac{\beta^2 Z^2 x^3}{4} - 2 - x + \frac{\beta Z x}{2}\left(2x + x^2\right)\right] + P\left(\frac{3}{2}x + 1\right) + \tilde{Z}\left(1 + x\right)^3 - M_0\right) = 0 \tag{3.44}$$

The remaining equation is a cubic polynomial that can be rewritten as:

$$\left(\tilde{Z}\left(\frac{3}{4}\beta Z + \frac{5}{2}\right)\right)x^3 + \left(6\tilde{Z}\right)x^2 + \frac{3}{2}\left(P - V_0^2 + \tilde{Z}\right)x + \left(P + \tilde{Z} - M_0 - 3V_0^2\right) = 0 \tag{3.45}$$

This equation can now be solved to find the remaining 3 steady state roots, x_0. The analytical solutions for this equation turn out messy, so the roots were calculated numerically. If we vary one parameter of the system and observe how the non-zero real roots change, we can see that saddle-node bifurcations occur where three real roots turn into one, or in the case of Figure 3.2 where one root turns into three.

The location of these bifurcations can be determined analytically. Let the left-hand side of (3.45) be $p(x)$. Since $p(x)$ is a cubic polynomial function, it will have either 1 or 3 real roots. Also, $p(x)$ will have a local maximum and a local minimum, $p(x_{max})$ and $p(x_{min})$.

The bifurcation occurs when either $p(x_{max})$ or $p(x_{min})$ crosses the x-axis, *i.e.* $p(x_{max}) = 0$ or $p(x_{min}) = 0$. Therefore, to determine this analytically we first must find the local extrema by taking the derivative of $p(x)$ with respect to x and finding the roots of the resulting quadratic equation.

$$\frac{dp(x)}{dx} = 3\tilde{Z}\left(\frac{3}{4}\beta Z + \frac{5}{2}\right)x^2 + 12\tilde{Z}x + \frac{3}{2}\left(P - V_0^2 + \tilde{Z}\right) = 0 \tag{3.46}$$

Therefore, the local extrema of (3.45) are:

$$x_{ext} = \frac{-8\tilde{Z} \pm \sqrt{-2\tilde{Z}\left[(P - V_0^2)(3\beta Z + 10) + \tilde{Z}(3\beta Z - 22)\right]}}{\tilde{Z}(3\beta Z + 10)} \tag{3.47}$$

Now, if we substitute x_{ext} into (3.45) we will get conditions depending on the parameters of the system that will show when the bifurcation occurs. Namely, when the following equation is satisfied:

$$\tilde{Z}\left(\frac{3}{4}\beta Z + \frac{5}{2}\right)x_{ext}^3 + \left(6\tilde{Z}\right)x_{ext}^2 + \frac{3}{2}\left(P - V_0^2 + \tilde{Z}\right)x_{ext} + \left(P + \tilde{Z} - M_0 - 3V_0^2\right) = 0 \tag{3.48}$$

For the simulation in Figure 3.2, u_0 was varied and the constant parameters used were:

$$h = 0.1,\ T = 1,\ \mu_0 = 1,\ \rho = 11,\ F_1 = 2,\ \alpha = 1,\ \beta = 3,\ \xi = 1 \tag{3.49}$$

When we use these parameters in (3.48) for x_{max} and solve for u_0 we get 4 imaginary solutions. On the other hand when we use x_{min} we get 2 real solutions: $u_0 = \pm 0.300895$. Looking at Figure 3.2 we can see that indeed the saddle-node bifurcation occurs at $u_0 = 0.300895$.

3.3.2 Linear Stability

We can now analyse the stability of the system around the critical points x_0. In order to do this, we will linearize the ODE around the critical points and study the linear stability. Let us take $x \to x_0 + \epsilon e^{r\tau}$ and only keep terms that are $\mathcal{O}(\epsilon)$ so that we will get a characteristic equation in terms of $r = r(x_0)$. Let equation (3.38) be a function $F(x, x', x'') = 0$. We know that, $x = x_0 + \epsilon e^{r\tau}$, $x' = r\epsilon e^{r\tau}$, $x'' = r^2\epsilon e^{r\tau}$, so we have $F(x_0 + \epsilon e^{r\tau}, r\epsilon e^{r\tau}, r^2\epsilon e^{r\tau}) = 0$. We also know that $F(x_0, 0, 0) = 0$ because x_0 is a steady state solution. Therefore, the linearization looks like:

$$\left.\frac{\partial F}{\partial x}\right|_{(x_0,0,0)} \cdot \epsilon e^{r\tau} + \left.\frac{\partial F}{\partial x'}\right|_{(x_0,0,0)} \cdot r\epsilon e^{r\tau} + \left.\frac{\partial F}{\partial x''}\right|_{(x_0,0,0)} \cdot r^2\epsilon e^{r\tau} = 0 \tag{3.50}$$

Computing the individual parts we get:

$$\begin{aligned}\frac{\partial F}{\partial x}\Big|_{(x_0,0,0)} &= 6\tilde{Z}x_0\left(1+x_0\right)^2 - 3V_0^2\left(1+x_0\right) + \\ &\quad 3\tilde{Z}x_0^2\left(1+x_0\right) + P\left(3x_0+1\right) + \tilde{Z}\left(1+x_0\right)^3 - M_0\end{aligned} \tag{3.51}$$

$$\frac{\partial F}{\partial x'}\Big|_{(x_0,0,0)} = 2V_0\beta Z x_0 + 2V_0 - V_0\beta Z x_0^2 - \frac{3}{2}\beta^2 Z^2 x_0^3 \tag{3.52}$$

$$\frac{\partial F}{\partial x''}\Big|_{(x_0,0,0)} = A + 1 + \beta Z x_0 \tag{3.53}$$

This equation can be solved analytically if we use the critical point $x_0 = 0$ in (3.50). We get the characteristic equation:

$$\left(A+1\right)r^2 + \left(2V_0\right)r + \left(P + \tilde{Z} - 3V_0^2 - M_0\right) = 0 \tag{3.54}$$

Using the quadratic equation to solve for r:

$$r_{1,2} = \frac{-V_0 \pm \sqrt{V_0^2 - \left(A+1\right)\left(P + \tilde{Z} - 3V_0 - M_0\right)}}{A+1} \tag{3.55}$$

We can now get conditions on when $x_0 = 0$ is stable, which occurs when the real part of both values of r are less than zero: $Re\left(r_{1,2}\right) < 0$.

Next, let us analyse the stability of the remaining equilibrium points. Using the same parameters as earlier (3.49), we increase u_0 and plot the location of the equilibrium points as a function of u_0. Then, we linearize around each equilibrium point for each value of u_0, find the characteristic equation and its roots, and plot the real parts of the 2 roots. This procedure can be seen in Figure 3.3, where the color of the lines of the equilibrium points correspond to the same color in the stability plot. We know that the equilibrium point is stable when the real part of both roots is less than 0. Therefore, we can look at Figure 3.3b and easily see where the stable equilibrium points, which is when either the single point or both points is completely under the line $Re\left(r\right) = 0$.

Take for example the black line in Figure 3.3b which corresponds to the permanent equilibrium point $x_0 = 0$. We can see that for values of $u_0 = 0.01$ to around $u_0 = 0.125$, the equilibrium point is stable. However, after $u_0 = 0.125$ the real part of one of its roots becomes greater than zero, so it is no longer stable. Furthermore, at the same point near $u_0 = 0.125$

Figure 3.3 Stability analysis of the stretching tube system as the fluid velocity, u_0, is increased from 0.01 to 0.5, with the parameters defined in (3.49).

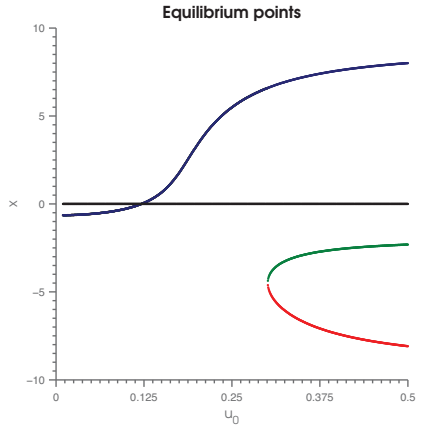

(a) All equilibrium points using the cubic polynomial (3.45), and including $x_0 = 0$.

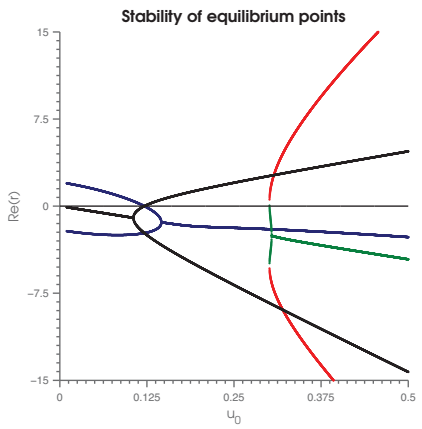

(b) Real part of the roots of the characteristic equation in (3.50).

the equilibrium point corresponding to the blue line turns from an unstable equilibrium to a stable one. We can see that this occurs in Figure 3.3a when the blue line intersects the black line at $x_0 = 0$. Therefore, there is always a non-negative stable equilibrium point for all positive u_0 for this choice of parameters.

Figure 3.3 agrees with the behaviour observed in Figure 3.1 and confirms the stability analysis. Looking at $u_0 = 0.5$ in the left subfigure of Figure 3.3, we see the stable equilibria at $x = 8$ and $x = -2.5$, and unstable equilibria at $x = 0$ and $x = -8$.

Let us now look at how the other parameters affect the stability. When we vary F_1 or ρ, a similar graph to Figure 3.3 is produced. However, when α is varied a different behaviour occurs. If we look at Figure 3.4, we can see that α has no effect on the position of the equilibrium points. Also, the stability of the equilibrium points do not change since no lines in Figure 3.4b ever cross $Re\,(r) = 0$. This is an expected result. Since the cubic polynomial (3.45) is independent of α, any change to α will not affect the position of the roots.

Next, we look at ξ in Figure 3.5. As ξ is varied, we observe a behaviour opposite to when u_0, F_1, and ρ were varied. That is, the equilibrium point $u_0 = 0$ begins as an unstable equilibrium for low values of ξ and as ξ is increased it turns into a stable point.

To further investigate this behaviour, let us plot the equilibrium points as a function of several parameters and observe the resulting surfaces. First, in Figure 3.6 we look at the

Figure 3.4 Stability analysis of the stretching tube system as the linear mass of the tube, α, is increased from 0.01 to 100, with the parameters defined in (3.49) and $u_0 = 1$.

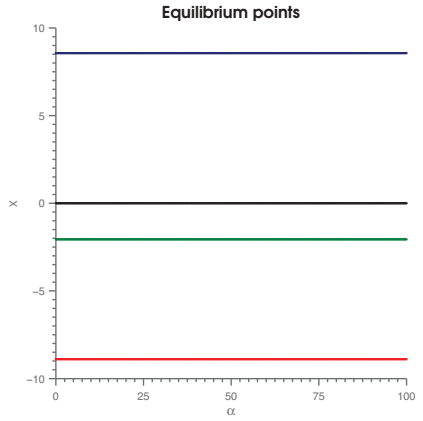

(a) All equilibrium points using the cubic polynomial (3.45), and including $x_0 = 0$.

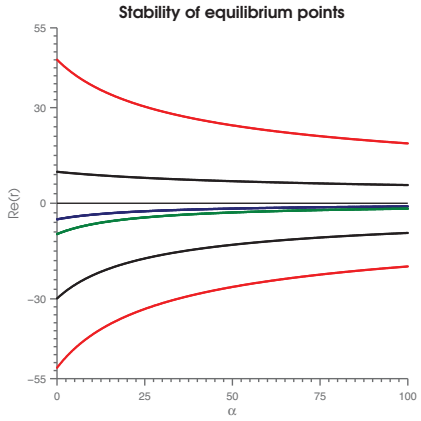

(b) Real part of the roots of the characteristic equation in (3.50).

equilibrium points as a function of u_0 and ξ. We can observe that if ξ is increased, u_0 must also be increased for a bifurcation to occur. The bifurcation can be observed in the bottom right corner with the two blue coloured surfaces. We also can look at Figure 3.7, which shows the surfaces of the equilibrium points as a function of ρ and u_0, to see a mirrored behaviour to Figure 3.6. As ρ is increased, the bifurcation occurs for smaller values of u_0.

We can also investigate the loss of stability of the equilibrium points as a function of 2 parameters. In Figure 3.8, the real roots of the characteristic equation are plotted as a function of u_0 and ξ. The equilibrium points in question are from the upper green and red surface in Figure 3.6. Stability occurs when the surface is completely below the plane $Re\,(r) = 0$. We observe that as ξ is increased, u_0 also must increase for the equilibrium point to become stable.

In Figure 3.3 and Figure 3.5, as the equilibrium point $x_0 = 0$ either gains or loses its stability another equilibrium point changes stability as well as it passes through $x = 0$. Let's look at this behaviour further by investigating the stability surfaces of the equilibrium points $x_0 = 0$ and the non-bifurcating equilibrium points that passes through $x = 0$ in Figure 3.9. The two surfaces intersect in a line inside the plane $Re\,(r) = 0$. This intersection happens at the same point when the non-bifurcating equilibrium points passes through $x = 0$. We can conclude from this that there is always a stable non-negative equilibrium point for all

positive ξ and u_0. As ξ is increased, the stable equilibrium point stays at $x_0 = 0$ for higher values of u_0 before it increases away from $x = 0$.

Conclusion

In closing, in this section we derive the equations of motion of a discrete fluid-conveying tube constrained to stretch in 1-dimension. This model consisted of a tube with 3 discrete points. The trajectory of the system was investigated and the stability was analyzed, including the location of saddle-node bifurcations. This model made use of a variational integrator that took into account a geometrically exact, dynamically changing cross sectional area of the tube.

Figure 3.5 Stability analysis of the stretching tube system as the stretch coefficient, ξ, is increased from 0.01 to 150, with the parameters defined in (3.49) and $u_0 = 1$.

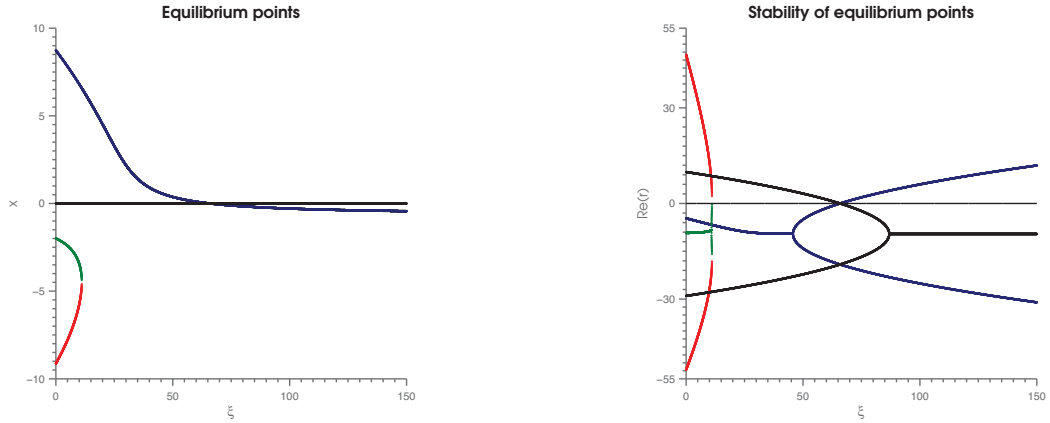

(a) All equilibrium points using the cubic polynomial (3.45), and including $x_0 = 0$.

(b) Real part of the roots of the characteristic equation in (3.50).

Figure 3.6 Surface of equilibrium points of the stretching tube system with the parameters defined in (3.49) as u_0 is varied from 0.01 to 1, and ξ is varied from 0.01 to 15. $x_0 = 0$ is an equilibrium point for all values.

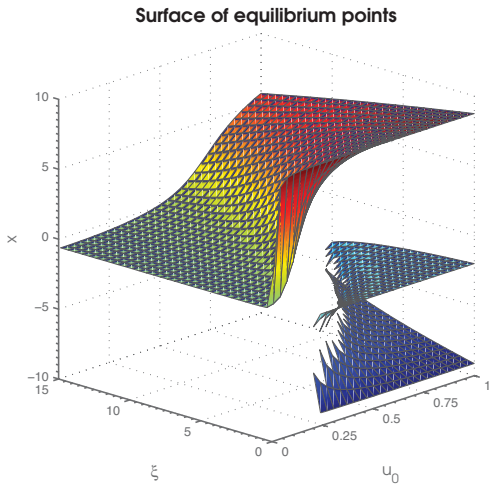

Figure 3.7 Surface of equilibrium points of the stretching tube system with the parameters defined in (3.49) as u_0 is varied from 0.01 to 1, and ρ is varied from 3 to 20. $x_0 = 0$ is an equilibrium point for all values.

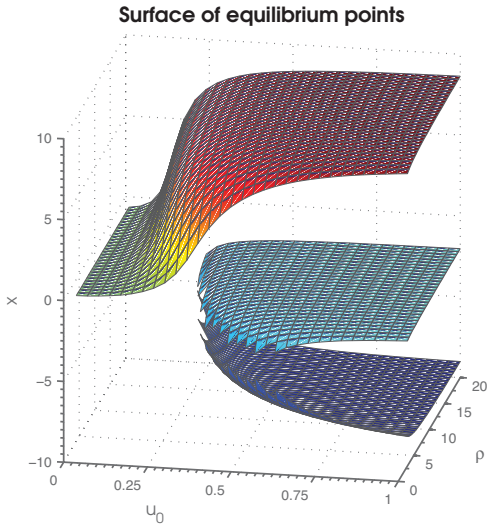

Figure 3.8 Surface of stability with the parameters defined in (3.49) as u_0 is varied from 0.01 to 1 and ξ is varied from 0 to 15. The gray surface corresponds to $Re\,(r) = 0$.

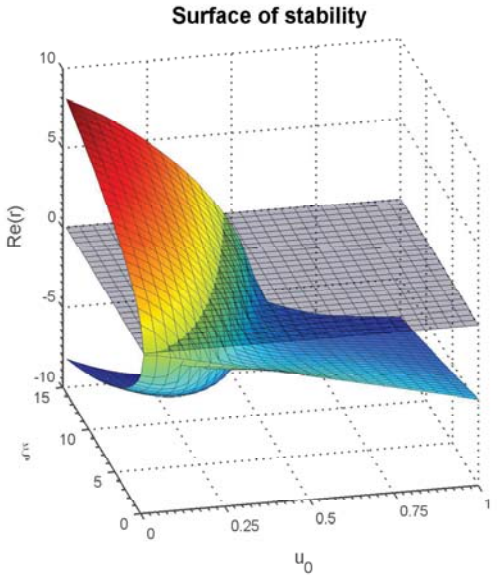

Figure 3.9 Surfaces of stability as u_0 is varied from 0.01 to 1 and ξ is varied from 0 to 15. The gray surface corresponds to $Re\,(r) = 0$. The blue surface corresponds to the equilibrium point $x_0 = 0$ and the red surface is the same as in Figure 3.8.

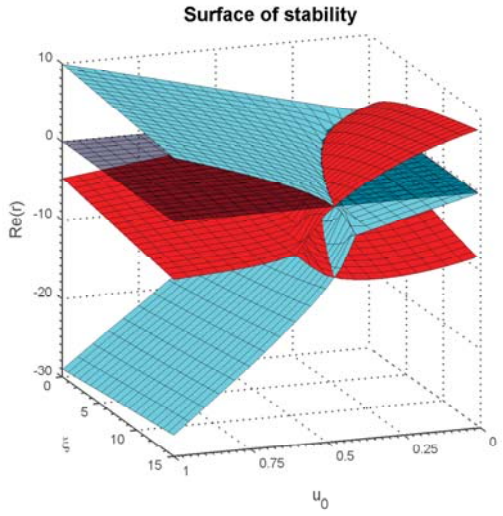

4 m - Point Discretization

Now, we will extend the 3-point discretization defined above, using all the same assumptions and constraints, to m-points. Again, since there is no twist $\lambda_i = Id$ and $\boldsymbol{\omega}_i = 0$ for all i. The tube position is now defined as:

$$\begin{aligned}
\mathbf{r}_0 &= 0 \\
\mathbf{r}_1 &= h + hx_1 \\
\mathbf{r}_2 &= 2h + hx_2 + hx_1 \\
&\vdots \\
\mathbf{r}_{n-1} &= (n-1)\,h + hx_{n-1} + \cdots + hx_1 \\
\mathbf{r}_n &= nh + hx_{n-1} + \cdots + hx_1
\end{aligned} \tag{4.1}$$

The linear strain is defined as:

$$\begin{aligned}
\boldsymbol{\kappa}_0 &= h + hx_1 \\
\boldsymbol{\kappa}_1 &= h + hx_2 \\
&\vdots \\
\boldsymbol{\kappa}_{n-2} &= h + hx_{n-1} \\
\boldsymbol{\kappa}_{n-1} &= h
\end{aligned} \tag{4.2}$$

The linear velocity is defined as:

$$\begin{aligned}
\boldsymbol{\gamma}_0 &= 0 \\
\boldsymbol{\gamma}_1 &= h\dot{x}_1 \\
\boldsymbol{\gamma}_2 &= h\dot{x}_2 + h\dot{x}_1 \\
&\vdots \\
\boldsymbol{\gamma}_{n-1} &= h\dot{x}_{n-1} + \cdots + h\dot{x}_1 \\
\boldsymbol{\gamma}_n &= h\dot{x}_{n-1} + \cdots + h\dot{x}_1
\end{aligned} \tag{4.3}$$

The cross-sectional area of the tube is defined as:

$$\begin{aligned} F_0 &= F_a - \frac{\beta}{2} h^2 x_1^2 \\ F_1 &= F_a - \frac{\beta}{2} h^2 x_2^2 \\ &\vdots \\ F_{n-2} &= F_a - \frac{\beta}{2} h^2 x_{n-1}^2 \\ F_{n-1} &= F_a \end{aligned} \tag{4.4}$$

4.1 Conservation Laws

We will use the same discrete Lagrangian defined earlier:

$$\ell = \sum_i \frac{1}{2} \left(\alpha \left| \boldsymbol{\gamma}_i \right|^2 + \langle \mathbb{I} \boldsymbol{\omega}_i, \boldsymbol{\omega}_i \rangle + \rho F(\boldsymbol{\kappa}_i, \lambda_i) \left| \boldsymbol{\gamma}_i + \frac{\boldsymbol{\kappa}_i}{h} u_i \right|^2 - \langle \mathbb{J} \lambda_i, \lambda_i \rangle - \xi \left| \frac{\boldsymbol{\kappa}_i}{h} - \boldsymbol{\chi} \right|^2 \right) \left| \frac{\boldsymbol{\kappa}_i}{h} \right| \tag{4.5}$$

$$\ell = \sum_i \mathcal{L}_i \left| \frac{\boldsymbol{\kappa}_i}{h} \right| \tag{4.6}$$

4.1.1 Fluid Volume

Using the fluid volume conservation law we can solve for u_i and $\dot{u}_i$.

$$u_i = u_{i-1} \frac{F_{i-1}}{F_i} + \frac{\beta h^3 x_i \dot{x}_i}{F_i}, \qquad i = 1, 2, ..., n-1 \tag{4.7}$$

$$\dot{u}_i = \frac{\beta h^3 \left(\dot{x}_i^2 + x_i \ddot{x}_i \right)}{F_i} - \frac{\beta h^2 u_{i-1} x_i \dot{x}_i}{F_i} \tag{4.8}$$

4.1.2 Linear Momentum

The linear momentum conservation law, taking into account that the tube doesn't twist, reads:

$$\frac{d}{dt} \left(\frac{\delta \ell}{\delta \boldsymbol{\gamma}_i} \right) + \frac{\delta \ell}{\delta \boldsymbol{\kappa}_i} - \mu_i \frac{\partial F_i}{\partial \boldsymbol{\kappa}_i} - \frac{\delta \ell}{\delta \boldsymbol{\kappa}_{i-1}} + \mu_{i-1} \frac{\partial F_{i-1}}{\partial \boldsymbol{\kappa}_{i-1}} = 0, \quad i = 1, 2, .., n-1 \tag{4.9}$$

Solving this equation analytically in terms of x_i becomes messy. We can however write the conservation law in terms of the above defined variables:

$$\begin{aligned}
&\tfrac{d}{dt}\left[\alpha\boldsymbol{\gamma}_i + \rho F\left(\boldsymbol{\kappa}_i, \lambda_i\right)\left(\boldsymbol{\gamma}_i + \tfrac{\boldsymbol{\kappa}_i}{h}u_i\right)\right]\left|\tfrac{\boldsymbol{\kappa}_i}{h}\right| + \\
&\left[\tfrac{1}{2}\rho\tfrac{\partial F_i}{\partial \boldsymbol{\kappa}_i}\left|\boldsymbol{\gamma}_i + \tfrac{\boldsymbol{\kappa}_i u_i}{h}\right|^2 + \tfrac{\rho F_i u_i}{h}\left(\boldsymbol{\gamma}_i + \tfrac{\boldsymbol{\kappa}_i u_i}{h}\right) - \tfrac{\xi}{h}\left(\tfrac{\boldsymbol{\kappa}_i}{h} - 1\right)\right]\left|\tfrac{\boldsymbol{\kappa}_i}{h}\right| + \\
&\mathcal{L}_i\tfrac{\boldsymbol{\kappa}_i}{h^2\left|\frac{\boldsymbol{\kappa}_i}{h}\right|} - \mathcal{L}_{i-1}\tfrac{\boldsymbol{\kappa}_{i-1}}{h^2\left|\frac{\boldsymbol{\kappa}_{i-1}}{h}\right|} + \mu_{i-1}\tfrac{\partial F_{i-1}}{\partial \boldsymbol{\kappa}_{i-1}} - \mu_i\tfrac{\partial F_i}{\partial \boldsymbol{\kappa}_i} - \\
&\left[\tfrac{1}{2}\rho\tfrac{\partial F_{i-1}}{\partial \boldsymbol{\kappa}_{i-1}}\left|\boldsymbol{\gamma}_{i-1} + \tfrac{\boldsymbol{\kappa}_{i-1}u_{i-1}}{h}\right|^2 + \tfrac{\rho F_{i-1}u_{i-1}}{h}\left(\boldsymbol{\gamma}_{i-1} + \tfrac{\boldsymbol{\kappa}_{i-1}u_{i-1}}{h}\right) - \tfrac{\xi}{h}\left(\tfrac{\boldsymbol{\kappa}_{i-1}}{h} - 1\right)\right]\left|\tfrac{\boldsymbol{\kappa}_{i-1}}{h}\right| = 0
\end{aligned} \tag{4.10}$$

Conclusion

In this section we briefly laid out the framework for a more complex model than the model in Section 3. This could be used to further analyze the behavior and stability of this system.

5 Experiment

In this section, we empirically investigate the motion of a vertically suspended tube. This section contains new material.

5.1 Experimental Set-up

An experiment was created to investigate the physical behaviour of the garden hose instability. The apparatus consists of a vertically suspended latex tube that is fixed in place at the top. Tap water was used as the fluid to pass through the tube. In order to achieve a smooth and steady flow of water with as little turbulence as possible a pressure tank was used to force the water through the tube. The pressure tank was filled with water and then was connected through a pressure regulator to a compressed air outlet in the lab. The regulator made sure that there is constant pressure inside the tank. The pressure differential between the pressure tank and the room pressure causes the water to be pushed through a valve located at the bottom of the pressure tank towards the flexible tube. This set-up was used to try to produce a smoother and more continuous flow of water through the tube, as opposed to a regular electric pump or a peristaltic pump. The turbulence from a pump might cause vortices or other structures which could affect how the tube behaves and we wanted to try to remove as many uncontrollable variables as possible. After the water leaves the tank is passes through an in-line flow meter before it reaches the flexible tube. The flow meter served to accurately control and measure the flow-rate of water.

The end of the latex tubes were connected to a fitting that could be screwed into a fixture at the top of the apparatus. Therefore, different tubes could be easily swapped into the apparatus. This allowed for observation on the effects of changing the parameters of the tube, such as wall thickness, cross sectional diameter and length.

The apparatus was fitted with a black backdrop to provide high contrast to the tube which was a lighter color. See Figure 5.1 for an image of the experiment.

Figure 5.1 Photograph of experimental apparatus. The water tank and regulator can be seen in the lower right of the image.

5.2 Centerline Detection Algorithm

An algorithm was designed in MATLAB to detect where the centerline of the tube was using a photograph of the tube. A photograph is a matrix where each pixel of the photo is an element of the matrix. In color photos, each element is given 3 values for every pixel corresponding to the intensity of the colors red, green, and blue. The image is then converted to grey scale, which removes all the hue and saturation information for each pixel but retains the luminance. This cuts down the 3 values on each element to a single value, where the higher the value the brighter the pixel is. So the black background in the experiment will have a low value, around 1-6, while the tube which is a lighter color will have a value around 100. The picture is cropped so it only shows the tube and the black background.

Now we want to find where the tube is for every value of z, which we define as the vertical axis. If we take a single row of pixels from the picture and look at the intensity it will look similar to the Figure 5.2a. The difference in intensity of the black background compared to the light tube is obvious. One can also observe that the center of the tube is not necessarily where the brightest pixel is, so we can not use the highest value pixel to find the center point. Instead, to accurately find the center point of the tube we perform a least-squared quadratic fit over the range of the tube width. This produces a quadratic equation $P(x) = ax^2 + bx + c$

Figure 5.2 Pixel intensity from a single row of a grey-scale photograph of a latex tube. Higher values indicate brighter pixels.

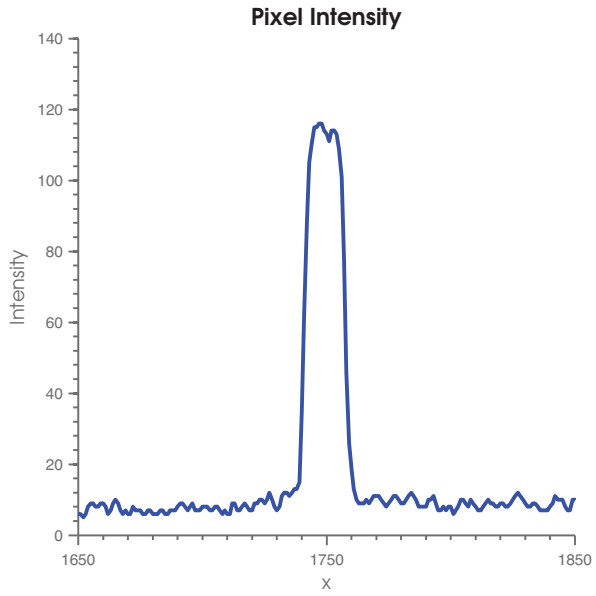

(a) Pixel intensity from a single row of an experimental photograph.

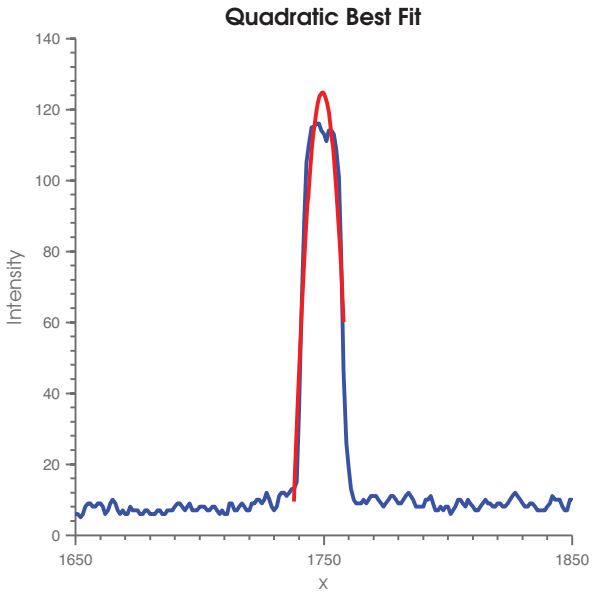

(b) Quadratic best-fit of pixel intensity represented by the red line.

and so we assumed the center-point of the tube to be the vertex of the parabola.

$$\begin{aligned} P(x) &= ax^2 + bx + c \\ P'(x) &= 2ax + b = 0 \\ x_{centerline} &= -\frac{b}{2a} \end{aligned} \tag{5.1}$$

An example of the quadratic best fit can be seen in Figure 5.2b. One can observe that the fit is a close approximation and the vertex provides a more accurate estimate of the center of the tube. This process repeats for every row of the photo until we get a curve which follows the centerline of the tube.

The output of the centerline detection algorithm can be seen in Figure 5.3. A photograph was always taken of the tube at rest before the experimental trial began. This ensured that the vertical axis of the output graph was parallel with gravity. The algorithm being run on the resting tube can be seen in Figure 5.3b. In this case, we see that the resting tube which should hang straight down is at a slight angle. If we subtract the values of this graph from the values of the unadjusted graph, then the final result in Figure 5.3c is the true orientation

Figure 5.3 Results of the centerline detection algorithm. The middle image of the resting centerline is used to adjust for potential rotation of the camera.

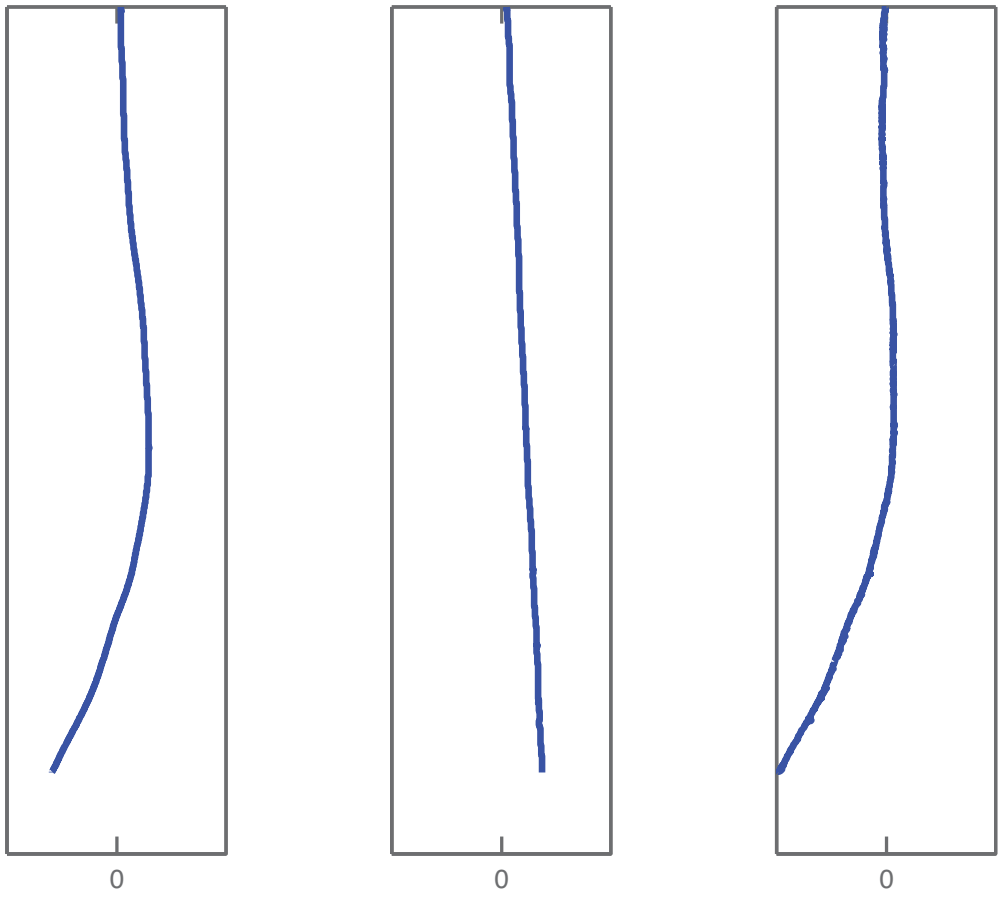

(a) Before adjustment. **(b)** Resting centerline. **(c)** After adjustment.

of the tube, with gravity parallel to the y-axis. This adjustment also works to center the top fixed end of the tube at exactly zero in the x-dimension.

5.3 Stereoscopic Camera

If only one camera is used to record the tube motion, then there is only information of the tubes orientation in 2-dimensions. In order to observe and record the 3-dimensional behaviour of the tube, a stereoscopic camera method was employed. Figure 5.4a provides a top-down view of the 2-camera system. The cameras had to be positioned with these exact specifications or else the following calculations will have large error.

An infra-red remote was used to trigger both cameras to take a photo simultaneously.

Figure 5.4 Schematic of the stereoscopic camera apparatus from the top and looking down.

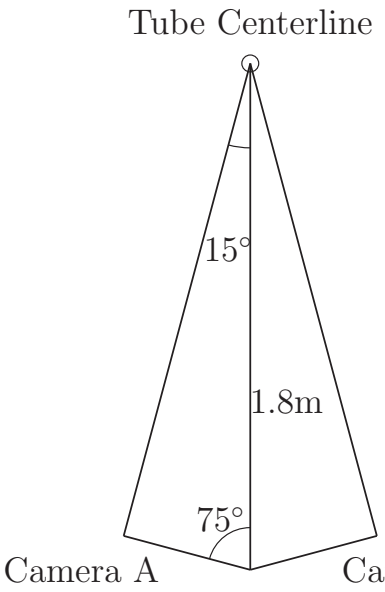

(a) Dimensions of the stereoscopic camera apparatus.

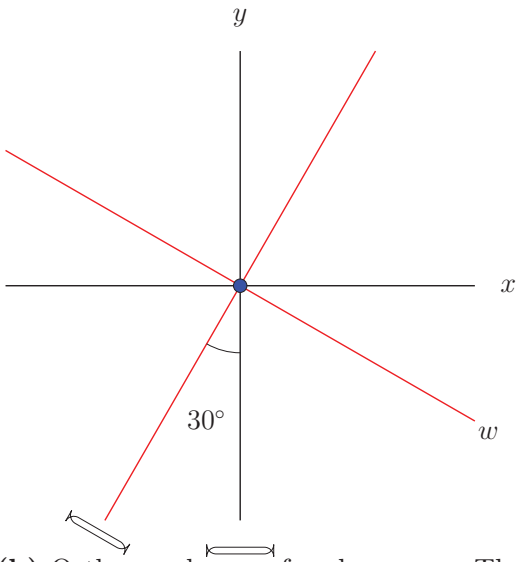

(b) Orthogonal axes of each camera. The cameras are represented by the boxes at the bottom of the figure.

Even though the cameras used were the same model, they still have small time differences between when they received the signal to take a photo and when the photo actually gets taken. The difference between the 2 cameras was measured to be less than 0.01 seconds.

5.3.1 3D - Coordinates

After we get a photo from each camera at the same time, we run the centerline detection algorithm on each photo. Since the cameras are not orthogonal to each other, we must perform calculations to determine the position of the tube in terms of the standard orthogonal basis (x, y, z), where z is the dimensional parallel with gravity. Figure 5.4b shows another top-down view of the axes we will use for the upcoming calculations. The blue dot represents the centerline of the tube at rest at a certain value of z, the height component. We define a line coming straight out of the right camera towards the tube to be the y-axis, and a perpendicular line going through the tube to be the x-axis. The line coming out of the left camera through the center of the tube is perpendicular to another axis that will be called the w-axis. These 2 sets of axes are offset by 30° by construction of the apparatus. The origin of both axes is the resting centerline of the tube.

In the following calculations we will assume infinite parallax, that is, we assume that the camera is infinitely far away from the tube so that all rays coming from the camera cross the respective axis at right angles. This can be visualized in Figure 5.5a. Similar to the above figure, the 2 cameras can be seen at the bottom of the illustration, at an angle of 30°. Now for this particular slice in the z-dimension, let the blue dot in the upper left quadrant be the current position of the tube after being deflected away from the resting position. The grey line coming from the left camera and intersecting the center of the tube is the true behaviour of light in the system. The blue line shows infinite parallax. One can imagine as the left camera gets pulled back away from the origin, the grey line approaches the blue line as the distance goes to infinity. The gray line crosses the w-axis at a point we define as P, and the blue line crosses the w-axis at a point we call Q. The distance from point P to the origin is the value of displacement that gets measured from the left camera using the centerline algorithm at this particular z. The infinite parallax assumption is that the distance from P to the origin is the same as the distance from Q to the origin. A similar assumption follows for the right camera.

$$d\left(P, O\right) = d\left(Q, O\right) \tag{5.2}$$

While it looks like there is quite a difference between these values in this diagram, in actuality the camera is much farther back and the tube deflection is small so the error in this assumption is much less.

With these assumptions in place, we can now begin the calculation. See Figure 5.5b for reference. First, we extend the line that is perpendicular to the w-axis through the center of the tube until it reaches the y-axis. Define this point of intersection as $y_{intercept}$. The point where this line intersects the w-axis is the value measured through centerline detection for the left camera for this particular z and we call this value w_d. We now draw a line that is perpendicular to the x-axis through the center of the tube. The point at which this line crosses the x-axis is the displacement computed through the centerline detection algorithm for the right camera for this particular z, we call this value x_d. The value we are trying to calculate is y_d so that we can write the position of the tube as (x_d, y_d, z) in terms of the orthogonal coordinate system relative to the right camera.

Figure 5.5 Top-down illustration of the 3-dimensional coordinates of the tube. The blue line is the behaviour of light if the camera was infinitely far away from the tube, and the grey line is the true behaviour of light coming into the camera.

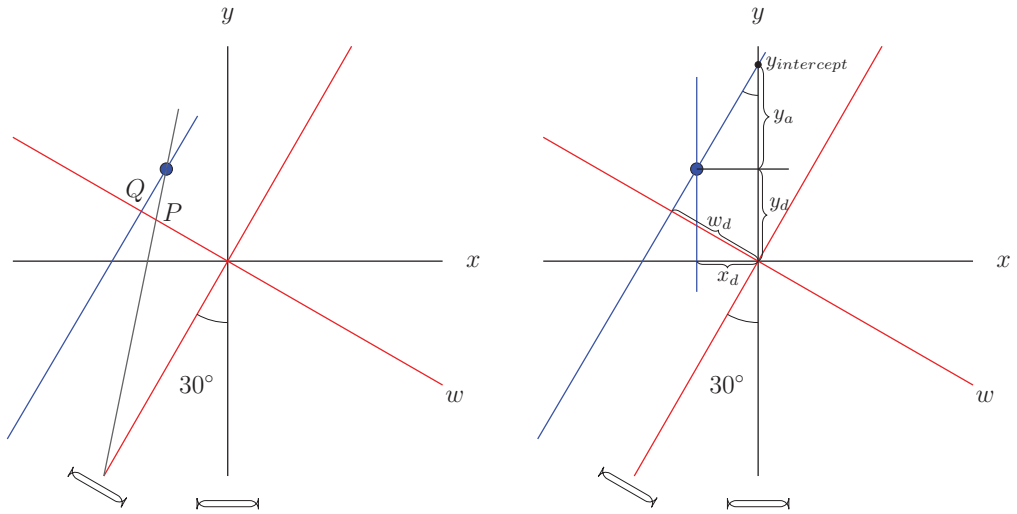

(a) Depiction of infinite parallax. **(b)** Diagram used to calculate y_d.

We first must calculate $y_{intercept}$ using simple trigonometry:

$$\begin{aligned} \sin(30°) &= -\frac{w_d}{y_{intercept}} \\ y_{intercept} &= -2w_d \end{aligned} \tag{5.3}$$

Where the negative sign ensures the correct sign of $y_{intercept}$. For the example in Figure 5.5b, w_d will have a negative value and $y_{intercept}$ needs to be positive. Next, using simple trigonometry again, we need to compute y_a and add it to $y_{intercept}$ to find the desired value y_d:

$$\begin{aligned} \tan(30°) &= \frac{x_d}{y_a} \\ y_a &= \sqrt{3}x_d \end{aligned} \tag{5.4}$$

Again looking at the example in Figure 5.5b, we see that x_d is negative so using the above equation y_a is negative as well. Therefore, we need to sum y_a and $y_{intercept}$ to get the correct value of y_d:

$$\begin{aligned} y_d &= y_a + y_{intercept} \\ y_d &= \sqrt{3}x_d - 2w_d \end{aligned} \tag{5.5}$$

Figure 5.6 Photograph of the rotating nozzle and motor used in the experiments to rotate the flexible tube conveying water.

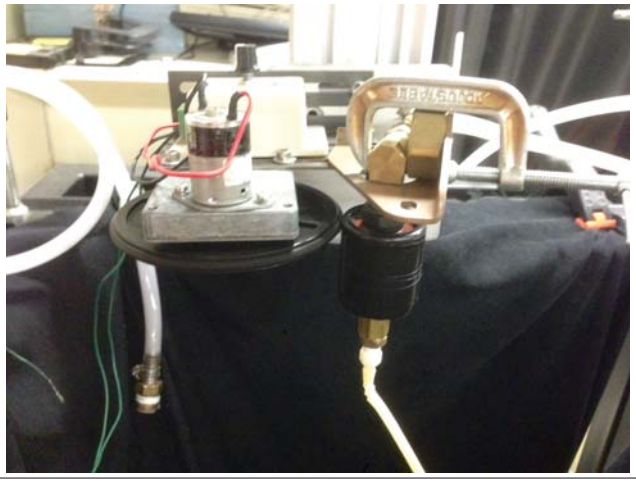

This simple calculation can be quickly repeated for each z and we will get a set of points (x_d, y_d, z) that represent the position of the tube in 3-dimensional space.

5.4 Stable Rotation

In observations of the experiment we noticed that during instability the tube would tend to twist back and forth with a constant frequency along the vertical axis of the tube. So we wondered if spinning the tube at a matching frequency would counteract this twist and stabilize the tubes instability. The apparatus used to rotate the tube can be seen in Figure 5.6.

A small DC motor attached to a gearbox with a large wheel attached on it was placed next to a rotating water nozzle. The rotating water nozzle was attached to the tube and allowed for free rotation of the tube without obstructing the flow of water. As the motor spun the wheel it would spin the rotary nozzle through friction alone. The gearbox increased the torque of the motor and also decreased the angular speed. In electric DC motors, the more voltage potential across the motor results in faster rotation speeds. Therefore, the motor was equipped with an LED dimmer switch that controls the voltage so that the speed of rotating could be controlled. In this set up, the motor could spin the tube anywhere from 0 Hz - 2 Hz. After running many tests with different flow rates and rotation speeds we noticed some interesting behaviour, namely stable fixed shape rotation. In Figure 5.7, one

Figure 5.7 Composite photographs demonstrating the rigid, fixed shape rotation of tube.

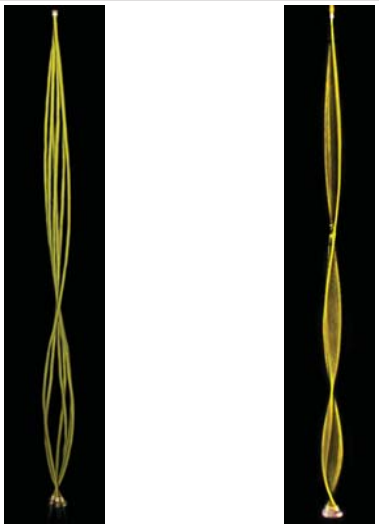

can observe this rigid rotation through composite photos. The tube rotates with relatively fixed shaped and depending on the parameters such as flow rate and rotation speed, it would either have 1, 2, or 3 fixed nodes.

Another example of this stabilization can be seen in Figure 5.8. The parameters in all 3 photos are the same except for the rotation speed. The left photo shows the normal behaviour of the tube with no forced rotation. The middle image shows small stabilization after being rotated since the deflection of the tube from the centerline is decreased. The right image shows the stable fixed rotation which occurs at a critical rotation speed. Any rotation speed higher or lower than the critical value will result in behaviour similar to the middle image.

5.5 The Koopman Operator

We now investigate if it is possible to predict what parameters will cause the stable rotation to occur. To do this, we take advantage of a linear operator known as the *Koopman Operator*. The Koopman operator is extensively discussed in [4]. For the following derivation, we closely follow the framework set out in [17].

The Koopman operator is an infinite-dimensional linear operator that exists for any non-linear dynamical system. It captures all the information of the non-linear dynamics of the system. This allows us to take advantage of linear spectral analysis without having to

Figure 5.8 Composite photographs of 3 tubes and rotational stabilization. The left image shows no forced rotation, the middle image shows some stabilization after forced rotation, and the right image shows rigid rotation at a critical rotation speed.

linearize the system. The Koopman operator allows one to decompose the motion of the tube in numerous modes. Say we have a time-discrete dynamical system on a manifold X such that:

$$\mathbf{x}_{m+1} = \mathbf{T}(\mathbf{x}_m), \quad \mathbf{x}_m \in X, \, \mathbf{T} : X \to X \tag{5.6}$$

Then the Koopman operator, K, for this dynamical system is defined by:

$$K(f(\mathbf{x})) = f(\mathbf{T}(\mathbf{x})) \tag{5.7}$$

where f is any scalar function $f : X \to \mathbb{R}$. One can confirm that this is a linear operator as well as an infinite-dimensional operator.

Now, we want to analyse the behaviour of the tube system using only the data obtained experimentally by finding the eigenvalues and eigenfunctions of K. Let $\phi_k : X \to \mathbb{R}$ be the eigenfunctions and $\lambda_k \in \mathbb{C}$ be the corresponding eigenvalues of K.

$$K\phi_k(\mathbf{x}) = \lambda_k \phi_k(\mathbf{x}) \tag{5.8}$$

Now, say we have some observable quantity of interest for the system, such as velocity at different points or, in the case of the experiment, the displacement from the resting centerline.

Let the observable be $\mathbf{f}$, where $\mathbf{f}$ is a vector valued function $\mathbf{f} : X \to \mathbb{R}^n$. If we assume that each component of $\mathbf{f}$ is in the span of the eigenfunctions ϕ_k, then we can write $\mathbf{f}$ as a linear combination of the Koopman eigenfunctions with vector coefficients $\mathbf{v}_k$.

$$\mathbf{f}(\mathbf{x}) = \sum_{k=1}^{\infty} \phi_k(\mathbf{x}) \mathbf{v}_k \tag{5.9}$$

It should be noted that if $\mathbf{f}$ is not in the span of eigenfunctions, then we have to split the operator up into its singluar and regular components and project these components of f onto the span of eigenfunctions ϕ_k. See [9].

We define $\mathbf{v}_k$ as the *Koopman modes* for the dynamical system map $\mathbf{T}$ for observable quantity $\mathbf{f}$. We also define ϕ_k as the *Koopman eigenfunctions* and λ_k as the *Koopman eigenvalues*. The Koopman modes will allow us to find the stable rotation shapes. The eigenvalues provide important information as they describe the temporal behaviour of their respective Koopman mode. From (5.6) and (5.7) we deduce that:

$$K\phi(\mathbf{x}_m) = \phi(\mathbf{x}_{m+1}) \tag{5.10}$$

In other words, applying the Koopman operator to the eigenfunction at a certain time step gives the eigenfunction at the next time step. So if we take the eigenfunction and Koopman mode decomposition equation in (5.9) of the observable $\mathbf{f}$ and use the previous equation:

$$\mathbf{f}(\mathbf{x}_m) = \sum_{k=1}^{\infty} \phi_k(\mathbf{x}_m) \mathbf{v}_k = \sum_{k=1}^{\infty} K\phi_k(\mathbf{x}_{m-1}) \mathbf{v}_k \tag{5.11}$$

Applying the Koopman operator m times:

$$\mathbf{f}(\mathbf{x}_m) = \sum_{k=1}^{\infty} K^m\phi_k(\mathbf{x}_0) \mathbf{v}_k = \sum_{k=1}^{\infty} \lambda_k^m\phi_k(\mathbf{x}_0) \mathbf{v}_k \tag{5.12}$$

From this, we can conclude that the Koopman eigenvalues affect the temporal behaviour of the Koopman modes. The problem now is that we don't explicitly know what the map $\mathbf{T}$ is for our dynamical system, and therefore we don't know what the Koopman operator is.

5.5.1 Arnoldi Algorithm as an Approximation for Koopman Modes

The algorithm laid out in [17] shows that one can get close estimates to the actual Koopman modes and eigenvalues without explicitly knowing the Koopman operator. All that is

required is snapshots of the system evolving in time, which is exactly the data we have for the rotating tube. The algorithm is as follows.

Let us define a linear dynamical system, $\mathbf{x}_{m+1} = \mathbf{A}\mathbf{x}_m$, $\mathbf{x}_m \in \mathbb{R}^n$. Let n be so much greater than m that the eigenvalues of A can't be calculated exactly. We will calculate estimates of these eigenvalues using a Krylov method. Starting with an initial vector, one computes the iterations $m-1$ times so we get a set of m vectors. The span of these vectors is called a Krylov subspace. We can take these m vectors, which are the observable data for each time step, and create a matrix $\mathcal{K}$.

$$\mathcal{K} = \begin{bmatrix} \mathbf{x}_0 & \mathbf{A}\mathbf{x}_0 & \mathbf{A}^2\mathbf{x}_0 & ... & \mathbf{A}^{m-1}\mathbf{x}_0 \end{bmatrix} \tag{5.13}$$

$$\mathcal{K} = \begin{bmatrix} \mathbf{x}_0 & \mathbf{x}_1 & \mathbf{x}_2 & ... & \mathbf{x}_{m-1} \end{bmatrix} \tag{5.14}$$

The idea is that if we project $\mathbf{A}$ onto the Krylov space, we will then be able to calculate the eigenvalues of the much smaller m dimensional matrix. In other words, we are trying to find the eigenvectors of $\mathbf{A}$ as linear combinations of the columns of $\mathcal{K}$. So we define this linear combination as:

$$\mathcal{K}\mathbf{c} = c_0\mathbf{x}_0 + \cdots + c_{m-1}\mathbf{x}_{m-1}, \quad \mathbf{c} = [c_0, \cdots, c_{m-1}] \tag{5.15}$$

If the m^{th} iteration is not a linear combination of the previous iterations, we get a residual:

$$\mathbf{r} = \mathbf{x}_m - \mathcal{K}\mathbf{c} \tag{5.16}$$

If $\mathbf{x}_m$ is a linear combination of the previous iterations, then $\mathbf{c}$ can be chosen such that $\mathbf{x}_m = \mathcal{K}\mathbf{c}$. Otherwise this residual is minimized if we choose $\mathbf{c}$ such that $\mathbf{r}$ is orthogonal to the span of the Krylov space. Now, we define a companion matrix $\mathbf{C}$, where the last column contains the coefficients $\mathbf{c}$ we found that minimize the residual.

$$\mathbf{C} = \begin{pmatrix} 0 & 0 & \cdots & 0 & c_0 \\ 1 & 0 & & 0 & c_1 \\ 0 & 1 & & 0 & c_2 \\ \vdots & & \ddots & & \vdots \\ 0 & 0 & \dots & 1 & c_{m-1} \end{pmatrix} \tag{5.17}$$

The eigenvalues of this companion matrix are an approximation of the actual eigenvalues of $\mathbf{A}$. Note that if the residual is 0 then the eigenvalues of $\mathbf{C}$ are no longer approximations and

are instead a subset of the eigenvalues of $\mathbf{A}$.

Now, we need to calculate the eigenvectors. The following equation holds true:

$$\mathbf{A}\mathcal{K} = \mathcal{K}\mathbf{C} + \mathbf{r}\mathbf{e}^T, \quad \mathbf{e} = [0, \cdots, 1] \in \mathbb{R}^m \tag{5.18}$$

So if $\mathbf{C}\mathbf{u} = \lambda\mathbf{u}$, then:

$$\mathbf{A}\mathcal{K}\mathbf{u} = \mathcal{K}\mathbf{C}\mathbf{u} + \mathbf{r}\mathbf{e}^T\mathbf{u} \tag{5.19}$$

$$\mathbf{A}\left(\mathcal{K}\mathbf{u}\right) = \lambda\left(\mathcal{K}\mathbf{u}\right) + \mathbf{r}\mathbf{e}^T\mathbf{u} \tag{5.20}$$

Therefore the approximate eigenvectors of A, called Ritz vectors, are $\mathbf{v} = \mathcal{K}\mathbf{u}$ and the approximate eigenvalues, called Ritz values, are λ. To put this algorithm to use we must find the $\mathbf{c}$ that minimizes the residual, in other words, we want $\mathbf{r} \perp span\left\{\mathbf{x}_0, \cdots, \mathbf{x}_{m-1}\right\}$. If 2 vectors are orthogonal then their dot product is 0. We want $\mathbf{r}$ orthogonal to each vector in the span, so we get a system of m equations:

$$\begin{aligned} \mathbf{x}_0 \cdot \left(\mathbf{x}_m - \mathcal{K}\mathbf{c}\right) &= 0 \\ \mathbf{x}_1 \cdot \left(\mathbf{x}_m - \mathcal{K}\mathbf{c}\right) &= 0 \\ \vdots \qquad & \qquad \vdots \\ \mathbf{x}_{m-1} \cdot \left(\mathbf{x}_m - \mathcal{K}\mathbf{c}\right) &= 0 \end{aligned} \tag{5.21}$$

This system can be reduced to:

$$\left(\mathcal{K}^T\mathcal{K}\right)\mathbf{c} = \begin{pmatrix} \mathbf{x}_0 \cdot \mathbf{x}_m \\ \mathbf{x}_1 \cdot \mathbf{x}_m \\ \vdots \\ \mathbf{x}_{m-1} \cdot \mathbf{x}_m \end{pmatrix} \tag{5.22}$$

We now can solve this system for $\mathbf{c}$, form the companion matrix $\mathbf{C}$, and get approximate eigenvalues and eigenvectors of A. [17] demonstrates that even for non-linear systems these eigenvalues λ are approximations of the true Koopman eigenvalues, and the eigenvectors $\mathbf{v}$ are approximations of the true Koopman Modes.

Before we can apply this to the data set of the rotating tube, we need to slightly modify the tube centerline data. When we take a picture of the tube at different times, where the

z component is in terms of the rows in the photo matrix doesn't necessarily correspond to the same physical point on the tube. We want to know how each physical point is evolving in the system in order to use the above algorithm. To do this we have to find the arc length of the tube position function using the following parametric arc length function.

$$\begin{aligned}\mathcal{L}(s) &= \int_0^n \sqrt{[x'(s)]^2 + [y'(s)]^2 + [z'(s)]^2}\,\mathrm{d}s \\ \mathcal{L}(s) &= \int_0^n \sqrt{[x'(s)]^2 + [y'(s)]^2 + 1}\,\mathrm{d}s\end{aligned} \tag{5.23}$$

The parameter s corresponds to the row number in the photo matrix where there are n rows. Since the z-coordinate is equivalent to the row number, $z'(s) = 1$. We now have a discrete function for the arc length as a function of the row number. Next, we must interpolate the inverse arc length function so that for equal increments of arc length, we can find what the corresponding z-coordinate is. For example, if we choose equal increments of 1, we can find z-coordinates by:

$$\begin{aligned}\mathcal{L}^{-1}(0) &= 0 \\ \mathcal{L}^{-1}(1) &= z_1 \\ &\vdots \\ \mathcal{L}^{-1}(1) &= z_n\end{aligned} \tag{5.24}$$

With these new z_i we interpolate again to find the new x_i and y_i. If we take a series of photos of the tube motion, we now know how the specific physical points on the tube are evolving in time. We now can form the Koopman matrix $\mathcal{K}$ using this data. Since we have information of the tubes displacement in 3 dimensions, we choose to stack the position vectors of $\mathbf{x}$, $\mathbf{y}$, and $\mathbf{z}$ in a column for each time step, seen in (5.25).

$$\mathcal{K} = \begin{pmatrix} \mathbf{x}_0 & \mathbf{x}_1 & \cdots & \mathbf{x}_{m-1} \\ \mathbf{y}_0 & \mathbf{y}_1 & \cdots & \mathbf{y}_{m-1} \\ \mathbf{z}_0 & \mathbf{z}_1 & \cdots & \mathbf{z}_{m-1} \end{pmatrix} = \begin{pmatrix} x_1^0 & x_1^1 & \cdots & x_1^{m-1} \\ \vdots & \vdots & & \vdots \\ x_n^0 & x_n^1 & \cdots & x_n^{m-1} \\ y_1^0 & y_1^1 & \cdots & y_1^{m-1} \\ \vdots & \vdots & & \vdots \\ y_n^0 & y_n^1 & \cdots & y_n^{m-1} \\ z_1^0 & z_1^1 & \cdots & z_1^{m-1} \\ \vdots & \vdots & & \vdots \\ z_n^0 & z_n^1 & \cdots & z_n^{m-1} \end{pmatrix} \tag{5.25}$$

5.5.2 Results

We can now begin to look for the Koopman modes and Koopman eigenvalues of the rotating tube system. For this example, we took 69 photos of the tube motion, at a time interval of 1 second. Following the algorithm above, we obtain the Koopman eigenvalues, Figure 5.9, and the Koopman modes, Figure 5.10. We see that most of the eigenvalues lie close to the unit circle. [9] states that the Koopman eigenvalues stay on the unit circle if the dynamical system is evolving on an attractor. This is true for the tube system as gravity and elasticity want to pull the tube back to a straight resting tube position. We can sort the modes and their respective eigenvalues by the magnitude of the mode, $||\mathbf{v}||$. The first Koopman mode with the largest magnitude corresponds to the time-averaged mean position of the tube, which we are not interested in. It can be seen as the pink dot in Figure 5.9. The next 4 leading Koopman modes and eigenvalues are shown in Figure 5.9 and 5.10 as the blue, red, green, and black dots or lines. The eigenvalues come in complex conjugate pairs for each leading mode.

As stated earlier, the eigenvalues define the frequency of oscillation for each Koopman mode. The Koopman modes can be thought of as shapes or structures of the tube that oscillate with their respective frequencies. The frequency is defined as follows:

$$\omega = \frac{Im\left[\log\left(\lambda\right)\right]}{\Delta t} \tag{5.26}$$

Figure 5.11 shows the frequencies and magnitudes of the leading Koopman modes. It is observed that the highest magnitude modes oscillate between 1 - 2 Hz. The main goal of this method is to see if stable rotation can be predicted by looking for shapes in the Koopman modes that match the shape and frequency of the stable rotation in experimental observations. In this example, it might be worth looking for stable rotation modes in the 1 - 2 Hz range. Further investigation is required.

Conclusion

To conclude, in this section we presented an experiment that was used to investigate the behaviour of a vertically suspended latex tube conducting water. Most interestingly, a stable rigid rotation was observed when the tube was forced to spin at a critical frequency. A stereoscopic camera along with a centerline detection algorithm was employed to obtain data on the motion of the tube in 3-dimensional space. We showcased a method to analyze the motion of a tube using the Arnoldi algorithm. The Arnoldi algorithm used empirical data of the motion of the tube and found the eigenvalues and eigenvectors of the Koopman operator. These can be used to find structures in the motion of the tube. Further investigation is required to determine the effectiveness of this procedure.

Figure 5.9 Koopman eigenvalues obtained using the Arnoldi algorithm and empirical data from the rotating tube.

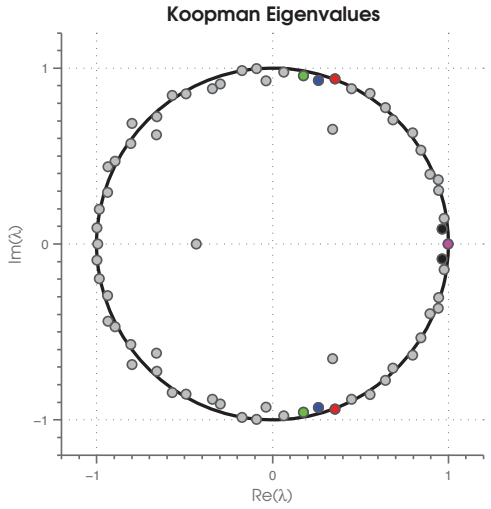

Figure 5.10 Four leading Koopman modes obtained using the Arnoldi algorithm and empirical data from the rotating tube.

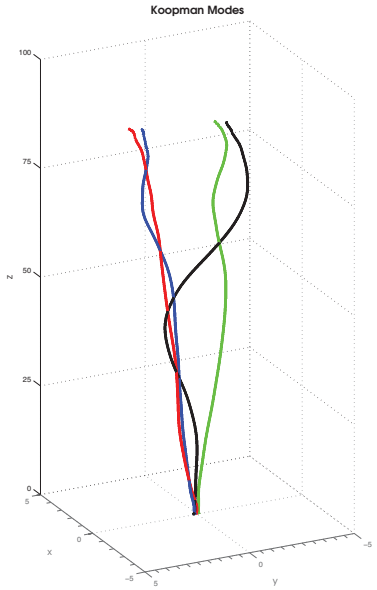

Figure 5.11 Frequency and magnitude of leading Koopman modes obtained using the Arnoldi algorithm and empirical data from the rotating tube.

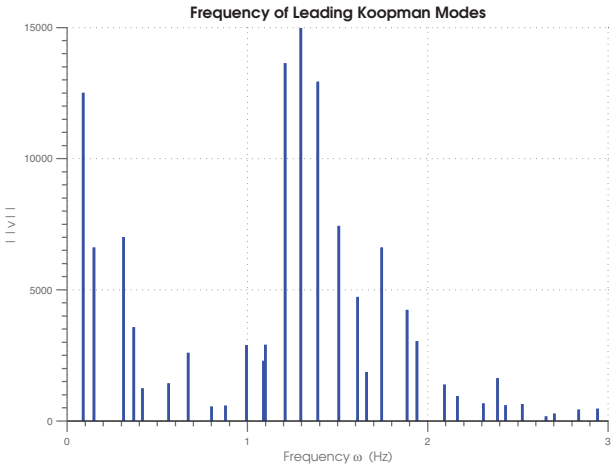

6 Conclusion

6.1 Discretized Stretching Tube

I have created a simple mathematical model of a flexible tube conveying a fluid using a variational approach that discretizes space. In my model, the tube's motion was restricted to one dimension and was not allowed to twist. The linear stability of this system was analyzed and conditions for stability were calculated analytically, including the location of equilibrium point bifurcation. This model utilized a geometrically exact, dynamically changing cross-sectional area theory which overcame previous shortcomings in other works. Further work could be done by experimentally investigating how well this model agrees with physical behavior. In the future, one could use the same variational integrator and relax the constraints used here, such as allowing the tube to move in 2 or 3 dimensions and also allowing twist. The conservation law for angular momentum would have to be used if twist was allowed. In the model above, the angular momentum equation had a trivial solution. One could also use the variational method discretizing both space and time set up in [7] and study the resulting equations. I briefly described the set up for an n-point discretization, but did not analyse the resulting behavior for this general case.

6.2 Empirical Analysis of Fluid-conveying Tubes

I have presented a method for studying the dynamics of the garden hose instability using empirical data. An experiment was designed and created that allowed for the motion of a vertically suspended flexible tube to be measured. The data collection method consisted of a stereoscopic camera to obtain the position coordinates of the tube in three dimensions, as well as a centerline detection algorithm which found the centerline of the tube from photographs.

The tube could also be forced to spin axially using a rotary nozzle. The appearance of rigid, fixed shape rotation was observed if the tube was spun with a specific rotation speed. Further investigation is required to quantify when this rigid rotation occurs in terms of flow rate and forced rotation speed. I then presented a means to analyse the collected data using spectral analysis of the Koopman operator. While this method has gained popularity in

studying flow dynamics in the field of fluid mechanics, it has not been used to analyse the garden hose instability. Further analysis is required to determine how effective this method is to study the dynamics of flexible tubes.

There are a few aspects of the experimental design that could be improved upon. It was not possible to get large sets of data which would improve the Koopman analysis. Currently, the experiment can only be run for a few minutes before the water tank runs out of water. This and the fact that the photos could not be taken at an interval faster than 1 second leads to around 60 time steps per experimental trial. This could be solved by using a more continuous source of water, or by increasing the size of the water tank. Also, a mechanism that allows the photos to be taken at faster intervals would allow for a greater amount of data to be collected.

References

[1] H. Ashley and G. Haviland. Bending vibrations of a pipe line containing flowing fluid. *Journal of Applied Mechanics-Transactions of the ASME*, 17(3):229–232, 1950.

[2] T.B. Benjamin. Dynamics of a system of articulated pipes conveying fluid. i. theory. In *Proceedings of the Royal Society of London A: Mathematical, Physical and Engineering Sciences*, volume 261, pages 457–486. The Royal Society, 1961.

[3] T.B. Benjamin. Dynamics of a system of articulated pipes conveying fluid. ii. experiments. In *Proceedings of the Royal Society of London A: Mathematical, Physical and Engineering Sciences*, volume 261, pages 487–499. The Royal Society, 1961.

[4] M. Budišić, R. Mohr, and I. Mezić. Applied koopmanism. *Chaos: An Interdisciplinary Journal of Nonlinear Science*, 22(4), 2012.

[5] F. Gay-Balmaz and V. Putkaradze. Exact geometric theory for flexible, fluid-conducting tubes. *Comptes Rendus Mécanique*, 342(2):79–84, 2014.

[6] F. Gay-Balmaz and V. Putkaradze. On flexible tubes conveying fluid: Geometric nonlinear theory, stability and dynamics. *Journal of Nonlinear Science*, 25(4):889–936, 2015.

[7] F. Gay-Balmaz and V. Putkaradze. Variational discretizations for the dynamics of fluid-conveying flexible tubes. *Comptes Rendus Mécanique*, 344(11):769–775, 2016.

[8] M.H. Ghayesh, M.P. Paıdoussis, and M. Amabili. Nonlinear dynamics of cantilevered extensible pipes conveying fluid. *Journal of Sound and Vibration*, 332(24):6405–6418, 2013.

[9] I. Mezić. Spectral properties of dynamical systems, model reduction and decompositions. *Nonlinear Dynamics*, 41(1-3):309–325, 2005.

[10] I. Mezic. Analysis of fluid flows via spectral properties of the koopman operator. *Annual Review of Fluid Mechanics*, 45:357–378, 2013.

[11] I. Mezić and A. Banaszuk. Comparison of systems with complex behavior. *Physica D: Nonlinear Phenomena*, 197(1):101–133, 2004.

[12] Y. Modarres-Sadeghi and M.P. Paıdoussis. Nonlinear dynamics of extensible fluid-conveying pipes, supported at both ends. *Journal of Fluids and Structures*, 25(3):535–543, 2009.

[13] M.P. Paidoussis. Flutter of conservative systems of pipes conveying incompressible fluid. *Journal of Mechanical Engineering Science*, 17(1):19–25, 1975.

[14] M.P. Paidoussis. *Fluid-Structure Interactions: Slender Structures and Axial Flow*, volume 1. Academic press, 1998.

[15] M.P. Paidoussis. *Fluid-Structure Interactions: Slender Structures and Axial Flow*, volume 2. Academic Press, 2004.

[16] M.P. Paidoussis and G.X. Li. Pipes conveying fluid: a model dynamical problem. *Journal of Fluids and Structures*, 7(2):137–204, 1993.

[17] C.W. Rowley, I. Mezić, S. Bagheri, P. Schlatter, and D.S. Henningson. Spectral analysis of nonlinear flows. *Journal of fluid mechanics*, 641:115–127, 2009.

[18] C. Semler, G.X. Li, and M.P. Paıdoussis. The non-linear equations of motion of pipes conveying fluid. *Journal of Sound and Vibration*, 169(5):577–599, 1994.

[19] J.C. Simo, J.E. Marsden, and P.S. Krishnaprasad. The hamiltonian structure of nonlinear elasticity: the material and convective representations of solids, rods, and plates. *Archive for Rational Mechanics and Analysis*, 104(2):125–183, 1988.